Cosmological Constraints on Sub-GeV Dark Vectors

by

John Coffey
B.Sc., University of Victoria, 2017

A Thesis Submitted in Partial Fulfillment of the
Requirements for the Degree of

MASTER OF SCIENCE

in the Department of Physics and Astronomy

Cosmological Constraints on Sub-GeV Dark Vectors

by

John Coffey
B.Sc., University of Victoria, 2017

Supervisory Committee

Dr. D. Morrissey, Co-supervisor
(Department of Physics and Astronomy)

Dr. A. Ritz, Co-supervisor
(Department of Physics and Astronomy)

Supervisory Committee

Dr. D. Morrissey, Co-supervisor
(Department of Physics and Astronomy)

Dr. A. Ritz, Co-supervisor
(Department of Physics and Astronomy)

Abstract

The purpose of this thesis is to recognize the effects of electromagnetic energy injection into the early Universe from decaying sub-GeV dark vectors. Decay widths and energy spectra for the most prominent channels in the sub-GeV region are calculated for various dark vector models. The models include the kinetic mixing of the dark photon with the Standard Model photon, $U(1)_{A'}$, a dark vector boson which couples to the baryon minus the lepton current, $U(1)_{B-L}$, and the last three are dark vector bosons which couple one lepton's current minus a different lepton's current, $U(1)_{L_i-L_j}$ where $i \neq j = e, \mu, \tau$. Measurements from Big Bang Nucleosynthesis and the Cosmic Microwave Background are used to constrain the lifetime, mass and coupling constant of the dark vectors.

Contents

List of Tables

List of Figures

Acknowledgments

I would like to thank:

Dr. David Morrissey, for being an amazing mentor, providing encouragement, being patient with all my questions, and allowing me to pursue a topic that I am truly passionate about.

Evan, Paul, Kyle and Zhelun for helping me get through all my classes.

Dedication

My mother, Katherine Coffey, for constantly supporting and encouraging my sister and I. Without you we would not be the people we are today.

Chapter 1

Introduction

This thesis studies the decay of sub-GeV dark vectors, specifically the effects of electromagnetic energy injections in the early Universe and constrains various dark vector models using measurements from Big Bang Nucelosynthesis and the Cosmic Microwave Background. The process of determining the effects comes from understanding the coupling of dark vectors to particles present in the Standard Model, which depends on what dark vector is being studied. The models include the kinetic mixing of the dark photon with the Standard Model photon, $U(1)_{A'}$, a vector which couples to the baryon minus the lepton current, $U(1)_{B-L}$, and the last three are vectors which couple to a lepton minus a different lepton current, $U(1)_{L_i-L_j}$ where $i \neq j = e, \mu, \tau$.

The procedure to find the energy spectra of the dark vectors begins with determining the decay width for each of the channels. Once found, the branching ratio for each model can be determined. The energy spectra for each of the channel can be computed for photons, and the sum of electrons and positrons. The three hadronic channels are the main focus of my work as the leptonic channels have been studied in great detail in the past. Combining both the branching ratios and energy spectra, constraints on the parameter space for the lifetime, coupling constant, and mass of dark vectors can be determined from Big Bang Nucleosynthesis and Cosmic Microwave Background measurements.

The thesis will follow the format:

Chapter 2 gives a brief review of the Standard Model, provides evidence for the existence of dark matter, describes the thermal relic abundance of cold dark matter production, describes methods of detection with current bounds and covers candidates of dark matter.

Chapter 3 covers sub-GeV dark vectors with all relevant decay channels, introduces various models to be tested and describes the energy spectra of electromagnetic particles produced from the decay of dark vectors. The decay channels of interest include $e^+e^-, \mu^+\mu^-, \pi^0\gamma, \pi^+\pi^-$ and $\pi^+\pi^-\pi^0$. The branching ratios for each model and energy spectrum for each channel are discussed and calculated.

Chapter 4 describes the application of the branching ratios and energy spectra to place new constraints on the parameter space of the lifetime, coupling constant and mass of dark vectors from measurements of Big Bang Nucleosynthesis and the Cosmic Microwave Background. Cosmic X-rays are also discussed and a lower bound for the lifetime of cold dark matter is found.

Chapter 5 concludes the thesis and discusses possible future work.

As a final note, my contributions to this project are described in Chapter 3. The calculated branching ratios and electromagnetic energy injection were used to determine the total electromagnetic energy injection from photons and electrons for the five models. These results were crucial for the analysis in Chapter 4, Sections 4.1 - 4.3, because the results were used by my collaborators, David Morrissey and Graham White, to constrain the models based on cosmological measurements. Section 4.4 was my primary contribution to Chapter 4 which examined a simplified model of the dark vector coupled to an exclusive e^+e^- decay.

Chapter 2

Review of the Standard Model and Dark Matter

2.1 The Standard Model: A Brief Review

The Standard Model (SM) was developed in the 60's and 70's and is the theory of fundamental particles and how they interact. The theory incorporates all known facts about discovered particles and was able to predict the existence of undiscovered particles [1, 2]. The paticles that form the SM are succinctly described in Table 2.1. It should be noted that not all the properties of the particles are shown. There are six leptons, six quarks, four force carriers, and the most recently discovered elementary particle in 2012, the Higgs Boson [3, 4]. The SM not only provides an excellent description of the weak, strong, and electromagnetic (EM) forces, but various particle physics experiments are overwhelmingly in agreement with the theory. The fourth fundamental force, gravity, is not described by the SM as it is exceedingly weak and almost always negligible for particle experiments, but plays a bigger role in other areas such as astronomy and cosmology.

The SM is gauge invariant under the gauge group $SU(3)_C \times SU(2)_L \times U(1)_Y$. The three groups each cover a different aspect of interactions of the particles. The $SU(3)$ group is responsible for governing strong interactions and the $SU(2)_L \times U(1)_Y$ spontaneously breaks to govern the electroweak force, a combination of the weak and EM forces. The fermionic particles in Table 2.1 transform under representations of these groups and their quantum numbers under these transformations are shown in Table 2.2

Fermions (Spin $\frac{1}{2}$)	**Mass**	**Electric Charge**	**Bosons** (Spin 0 or 1)	**Mass**	**Electric Charge**
Quarks			**Gauge Bosons** (spin = 1)		
Up (u)	2.16 MeV		Photon/EM (γ)	0	0
Charm (c)	1.27 GeV	$+\frac{2}{3}$			
Top (t)	172.9 GeV		Gluon/Strong (g)	0	0
Down (d)	4.67 MeV		Weak Force		
Strange (s)	93 MeV	$-\frac{1}{3}$	$W^{\pm}$	80.4 GeV	± 1
Bottom (b)	4.18 GeV		Z	91.2 GeV	0
Charged Leptons			**Scalar** (spin = 0)		
Electron (e)	0.511 MeV				
Muon (μ)	106 MeV	-1	Higgs (h)	125 GeV	0
Tau (τ)	1.8 GeV				
Neutrinos					
ν_e					
ν_μ	0^*	0			
ν_τ					

Table 2.1: Elementary particles of the SM with their respective approximate masses and electric charges in units of the proton charge e.

The quantum numbers indicate the representation of the appropriate $SU(N)$ group. If the quantum number is N then this is the fundamental representation, and if it is 1 this is the trivial representation which means it does not transform under the group. The adjoint representation is defined by the structure constants that define the Lie Algebra the SM utilizes to represent the gauge fields.

The gauge fields for the SM are shown in Table 2.3 and the SM Lagrangian is built around various gauge invariances:

$$\mathcal{L}_{SM} = \mathcal{L}_{Gauge} + \mathcal{L}_{Higgs} + \mathcal{L}_{Yukawa}. \tag{2.1}$$

*The matter content in Table 2.1, gauge invariance and renormalizability of the SM predicts that neutrinos are massless. However, neutrinos have experimentally been determined to have a small mass and the exact origin of their mass is unknown [5, 6, 7].

Fermion	Quantum Number $(SU(3)_c, SU(2)_L, U(1)_Y)$
$Q_L^i = \begin{pmatrix} u_L^i \\ d_L^i \end{pmatrix}$	$(3, 2, \frac{1}{6})$
u_R^i	$(3, 1, \frac{2}{3})$
d_R^i	$(3, 1, -\frac{1}{3})$
$L_L^i = \begin{pmatrix} \nu_L^i \\ e_L^i \end{pmatrix}$	$(1, 2, -\frac{1}{2})$
e_R^i	$(1, 1, -1)$
Scalar	
$H = \begin{pmatrix} H_1 \\ H_2 \end{pmatrix}$	$(1, 2, \frac{1}{2})$

Table 2.2: Representations of the SM fields with their quantum numbers when acted upon by the gauge groups. The i denotes the generation and all fermions within the same generation have the same quantum numbers. The last row is the Higgs doublet which is the only scalar to be discovered for the SM.

Gauge Field	Quantum Number $(SU(3)_c, SU(2)_L, U(1)_Y)$
G_μ^a	$(8, 1, 0)$
W_μ^p	$(1, 3, 0)$
B_μ	$(1, 1, 0)$

Table 2.3: G_μ^a is the adjoint representation of $SU(3)_c$ with $a = 1, ..., 8$ and described by the fundamental representations of this group, the Gell-Mann matrices. Similarly, W_μ^p is the adjoint representation of $SU(2)_L$, where $p = 1, 2, 3$ and described by their fundamental representation of the group, the Pauli matrices.

Examining each part of the Lagrangian,

$$\begin{aligned} \mathcal{L}_{Gauge} = &-\frac{1}{4}(G_{\mu\nu}^a)^2 - \frac{1}{4}(W_{\mu\nu}^p)^2 - \frac{1}{4}(B_{\mu\nu})^2 \\ &+ \bar{Q}_L i\gamma^\mu D_\mu Q_L + \bar{u}_R i\gamma^\mu D_\mu u_R + \bar{d}_R i\gamma^\mu D_\mu d_R \\ &+ \bar{L}_L i\gamma^\mu D_\mu L_L + \bar{e}_R i\gamma^\mu D_\mu e_R \end{aligned} \tag{2.2}$$

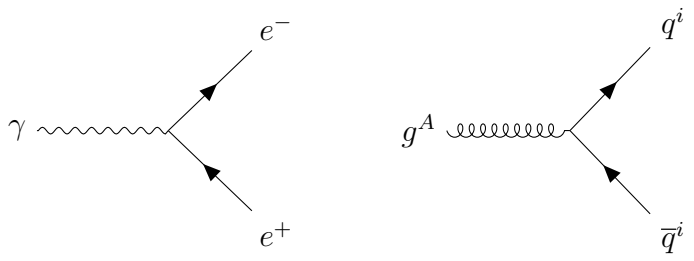

Figure 2.1: Feynman diagram of vertices for a photon interacting with an electron and positron (left) and a gluon interacting with a quark and antiquark (right). The indicies $i, j = 1, 2, 3$ are the colours red, green, and blue present for strong interactions only. $A = 1, ..., 8$ for the 8 types of gluons.

$$D_\mu = \partial_\mu + ig_s t^a_{r,c} G^a_\mu + igt^p_{r,L} W^p_\mu + ig' Y B_\mu \tag{2.3}$$

Where $F^a_{\mu\nu} = \partial_\mu F^a_\nu - \partial_\nu F^a_\mu - g_i f^a_{bc} F^b_\mu F^c_\nu$ is the field strength tensor definition for the three gauge field, $G^a_{\mu\nu}$, $W^p_{\mu\nu}$ and $B_{\mu\nu}$ are the gauge fields that couple to coloured, left-handed, and hypercharged fermions respectively, g_i corresponds to the coupling constant for each gauge group, f^{abc} is the structure constant dependent on the gauge group, $t^a_{r,c}$ represent the appropriate generators for $SU(3)_c$, $t^p_{r,L}$ are the appropriate generators for $SU(2)_L$, and Y is the hypercharge of the field under $U(1)_Y$.

The Higgs component is comprised of

$$\mathcal{L}_{Higgs} = \Big|\Big(\partial_\mu + ig\frac{\sigma^p}{2} W^p_\mu + ig'\frac{1}{2} B_\mu\Big) H\Big|^2 - \Big(-\mu^2 |H|^2 + \frac{\lambda}{2}|H|^4\Big) \tag{2.4}$$

Where σ^p are the Pauli Matrices, μ is dimensionful, and λ is dimensionless. The Higgs potential is the second term in round brackets and minimizing this potential imposes a condition of the gauge invariant combination of $|H|^2 \equiv H^\dagger H$. Utilizing gauge invariance it is most convenient to choose the unitary gauge, and expanding around it gives

$$H(x) = \begin{pmatrix} 0 \\ v + h(x)/\sqrt{2} \end{pmatrix} \tag{2.5}$$

Where $v = \sqrt{\mu^2/\lambda}$ is called the vacuum expectation value (vev) and is an important quantity. By placing the unitary gauge into the kinetic term of the Higgs component the masses for $W^\pm$, Z, and photon can be obtained. This is known as the Higgs Mechanism.

The masses of the gauge bosons can be found using only the Higgs component

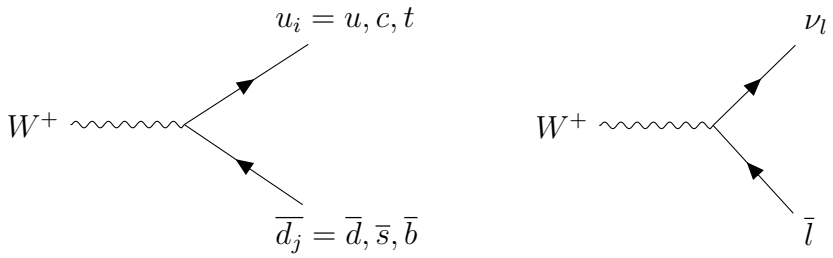

Figure 2.2: Feynman diagram of a W boson flavour-changing interaction between quarks (left) and a flavour-conserving interaction for leptons (right). The terms u_i and d_j are the quark generations, and $l = e, \mu, \tau$ the three generations of the leptons. The W boson can only interact with left-handed particles.

while the Yukawa term is necessary to obtain the mass of the fermions.

$$\mathcal{L}_{Yukawa} = -y_u \bar{Q}_L \tilde{H} u_R - y_d \bar{Q}_L H d_R - y_e \bar{L}_L H e_R + h.c \tag{2.6}$$

The Yukawa component corresponds to scalar-fermion Yukawa interactions where $\tilde{H} = i\sigma^2 H$, and y_i are the Yukawa coupling constants. Substituting the unitary gauge in the Yukawa component, the masses for the fermions can be calculated:

$$m_i = y_i v. \tag{2.7}$$

Thus, the larger the mass of the particle the higher the coupling to the Higgs particle. This is why many experiments are focused on large mass particles, in order to have more interactions with the Higgs boson [8].

The interactions described through the SM Lagrangian can be illustrated by Feynman diagrams. The probability of observing the results of the interactions can be expressed through this useful formalism. Depending on the force chosen the rules to construct Feynman diagrams will vary and may be derived from various Quantum Field Theory textbooks [9, 10].

The particles can interact with the appropriate force if they are not in the trivial representation of that group. For example, two electrons can not interact through a gluon since they do not possess colour. Figures 2.1, 2.2 and 2.3 are some examples of basic interactions one would see in EM, strong, and weak interactions. There are many more interactions but most Feynman diagrams can be built off of these vertices and the probability of observing these events can be calculated.

To summarize, the SM is a powerful tool and was built using gauge groups which

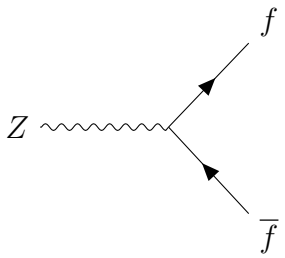

Figure 2.3: Feynman diagram of a Z boson neutral flavour-conserving interaction between any two SM fermions.

helped immensely in predicting particles. However, some phenomena can not be explained by the SM. Why are there only three distinct groups of leptons and quarks? How does one analytically calculate quark/gluon confinement? Why are there no right-handed neutrinos? But perhaps one of the biggest questions that seems to evade all answers: how to incorporate dark matter into the SM?

2.2 Evidence for Dark Matter

Dark matter was first conjectured over 80 years ago and defined as non-luminous matter that weakly interacts with visible matter. Due to the weak interactions of dark matter it has yet to be detected. Even though there has been no direct detection of dark matter, there is overwhelming observational evidence that suggests dark matter is present in the Universe.

2.2.1 Rotation Curves

To begin, one can examine the Universe around us or more specifically the galaxies around us. Galaxies are building blocks of the Universe where matter resides and come in various forms: dwarf, satellite, group, and so on. There are also clusters which are collections of galaxies bound by their mutual gravitational attraction. In the 1930's, Fritz Zwicky applied the Virial Theorem to the Coma Cluster. He observed the velocities of the galaxies within the Coma Cluster, and found that they were too high to be bound gravitationally by the visible matter. In his paper, he proposed that if luminous (visible) matter and non-luminous (dark) matter were summed when determining the mass, a significantly higher density could be achieved and explain why the galaxies in the cluster remain bounded [11].

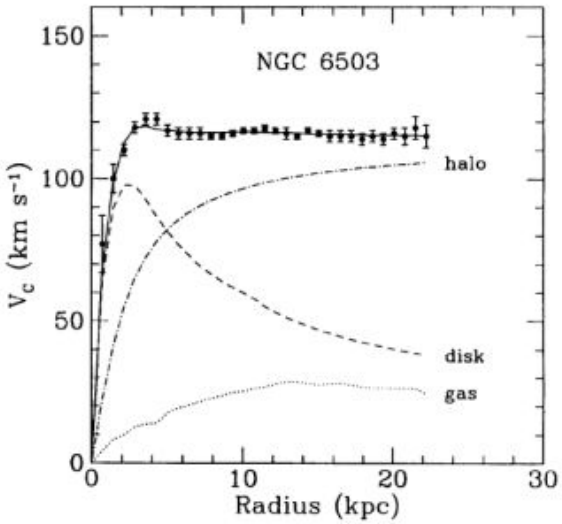

Figure 2.4: Galactic rotation curve of NGC 6503 showing disk and gas contributions plus the dark matter halo contribution required to match the observed data. Image Credit: [12]. Copyright ©1991 Royal Astronomical Society.

In the 1970's Vera Rubin and others studied the rotation curves of individual galaxies. They ascertained that rotation curves are flat as one moves away from the centre of the galaxy shown in Figure 2.4. This was quite exciting as this was a contradiction between observable results and Newtonian mechanics. To better understand the excitement consider a system where one mass is much larger than the other, $M \gg m$, the centre of mass frame is chosen (the same as the frame where M is at rest), the only force is the gravitational attraction between the two objects, and the smaller object moves with some centripetal acceleration $a = v^2/r$.

$$\frac{GMm}{r^2} = m\frac{v^2}{r} \Rightarrow v = \sqrt{\frac{GM}{r}} \tag{2.8}$$

If one is to assume that all of the mass M is near the centre, then after the threshold where all the mass is within a radius r, the velocity would follow $v \propto r^{-1/2}$. This was not found in the experiment, instead v is almost constant beyond that threshold and the only explanation was that the mass is dependent on the radius of the system, $M = M(r) \propto r$. Thus, there is mass that is not being taken into account on the outside of galaxy rotation curves. This unaccounted mass was called a dark halo which is where all the dark matter is said to be present and has a mass density $\rho \propto 1/r^2$, or equivalently $M(r) \propto r$ outside the threshold. The dark halo behaves differntly from

visible matter inside the threshold as can be seen in Figure 2.4. Galaxies like the Milky Way have a dark halo which contain about 90% of its mass [13, 14].

2.2.2 Bullet Cluster

Another piece of evidence for dark matter can be found upon examining the Bullet Cluster shown in Figure 2.5. The figure depicts the aftermath of two clusters colliding. If the galaxies were comprised of only visible matter one would expect the mass distribution to be largest at the centre of the collision. To see if this was true, the collision site of the galaxies was examined with two techniques.

The first technique examines the X-rays emitted from the collision that must come from visible matter. The Hubble Space Telescope and Chandra X-ray Observatory were able to obtain data from the cluster. The two collaborations looked for the brightness in the X-rays emitted, determined how energetic the X-rays were and where the source of the X-rays was located. Their findings are coloured red in Figure 2.5. As expected the visible matter is contained near the centre of the collision.

The second technique of observing the distribution of mass was performed with gravitational lensing. This technique does not depend on visible radiation and determines where large masses are located. From the principles of General Relativity, one can find that light bends when it passes by objects with a large mass. The large mass can act as a lens in the Universe and can focus light. Gravitational lensing effects of the Bullet Cluster are coloured blue in Figure 2.5, showcasing the location of two large masses.

If the two observational methods overlapped, one may conclude no dark matter is present in the Bullet Cluster. However, these two techniques clearly indicate that the visible matter is not where the majority of the mass is located. One can summarize that dark matter interacts with its surroundings on a much smaller scale than visible matter and during collision dark matter barely interacts with visible matter.

Figure 2.5: The Bullet Cluster coloured to emphasize the effect. The red is the visible matter clumped at the centre of the cluster, and the blue is the non-visible matter responsible for gravitational lensing. Image Credit: X-ray: NASA/CXC/CfA/M. Markevitch et al.; Lensing Map: NASA/STScI; ESO WFI; Magellan/U.Arizona/D.Clowe et al.; Optical: NASA/STScI; Magellan/U.Arizona/D.Clowe et al.. Obtained from APOD.

2.2.3 The Cosmic Microwave Background

The Cosmic Microwave Background (CMB) also supports the existence of dark matter and it would be beneficial to discuss where the CMB originated, starting from the beginning.

Observations give strong evidence that the Universe began with a period of inflation, then reheating and has been expanding ever since. Inflation generated fluctuations in the temperature and energy of photons at this time. The early Universe had an extraordinary amount of energy, and was at an extremely high temperature. At these high temperatures, annihilation and decay of heavy exotic particle could easily be reversed leading to the production of said particles. The destruction and creation of the particles lead to an equilibrium that could be maintained at these temperatures. As the Universe expanded, the temperature dropped and the production of the heavy exotic particles dropped substantially, while the annihilation and decay continued. After some time the Universe was cool enough to have protons and neutrons fuse together to form light elements, this was called Big Bang Nucleosynthesis

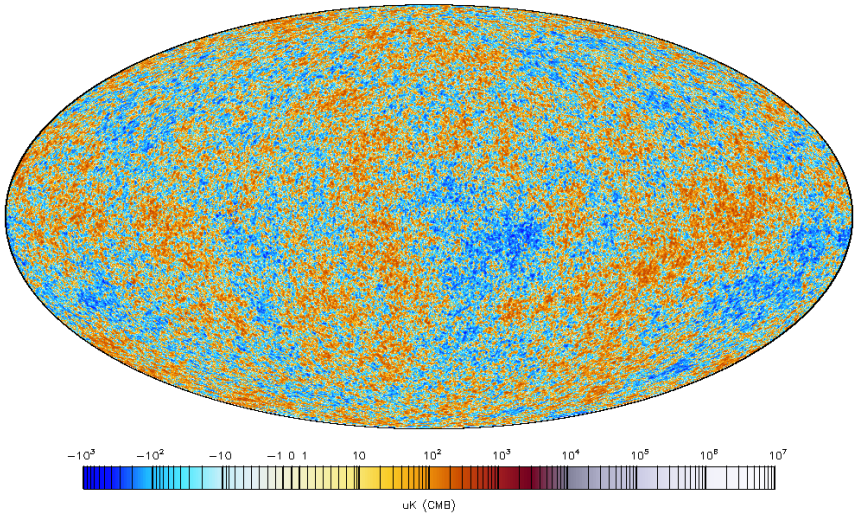

Figure 2.6: Planck all-sky picture reveals 13.77 billion year old temperature fluctuations. Image Credit: ESA and the Planck Collaboration

(BBN). The abundance of the light elements predicted by BBN agree very well with measurements and can be compared to the abundance of the elements to today in terms of a single parameter, the baryon to photon ratio, η_B.

The newly formed nuclei, henceforth referred to as baryons, in the early Universe coupled to photons. As the Universe expanded, these coupled baryons exerted pressure and began to oscillate. Baryon acoustic oscillations (BAO) measurements show the time when the oscillations turned off and coincide with the baryons decoupling from the photons and bonding with electrons. Thus, photons could freely propagate in the Universe and formed the CMB. The fluctuations (seeded by inflation) of the photons produced regions of high and low density resulting in gravity pulling baryonic and dark matter into dense regions [15]. At this point in time matter and radiation density were equal, known as matter-radiation equality, and the overdense regions start to self-gravitate, collapse and oscillate forming structures. The CMB captures the temperature and energy anisotropies of the photons that decoupled from the baryons.

The CMB was accidentally discovered in 1964 by Arno Penzias and Robert Wilson and the anisotropies of the CMB were first detected in 1992 by the COBE satellite [16]. Since then, the power spectrum of the CMB has been measured more precisely by more advanced spacecraft: WMAP (2001 - 2010) [17] and Planck (2009 - 2013) [18]. The all-sky map of the CMB can be seen in Figure 2.6 and the temperature

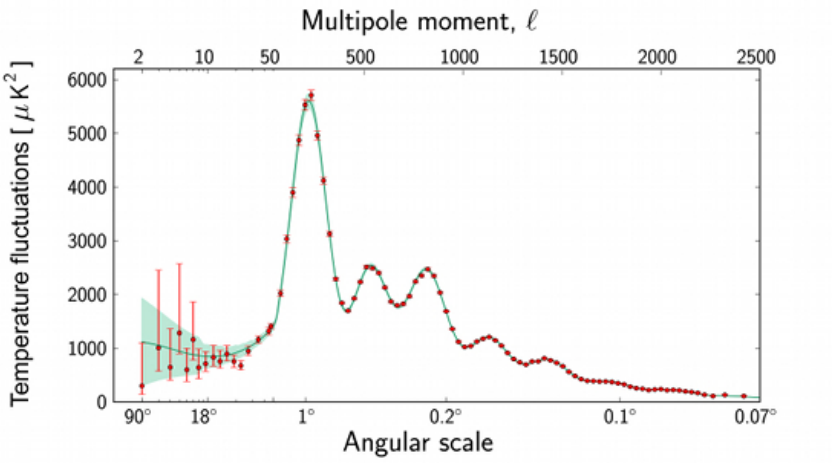

Figure 2.7: Planck CMB temperature power spectrum of the Planck full-sky map. The base-ΛCDM theoretical spectrum is plotted in light blue. Image Credit: ESA and the Planck Collaboration

fluctuation power spectrum is shown in Figure 2.7 from the most recent Planck measurements. The temperature fluctuations can be expressed as a power series with spherical harmonics

$$\frac{\delta T}{T}(\theta, \varphi) = \sum_{l,m} a_{l,m} Y_{l,m}(\theta, \varphi) \tag{2.9}$$

The ensemble average of the power series is normally plotted

$$C_l = \langle |a_{lm}|^2 \rangle = \frac{1}{2l+1} \sum_{m=-l}^{l} |a_{l,m}|^2 \tag{2.10}$$

The data obtained from these experiments have set tight constraints on parameters of the SM, which include the energy density distribution in the Universe. The present distribution of energy density is 4.8% visible matter, 26.0% dark matter, and 69.2% dark energy, the theoretical force that is responsible for the accelerated expansion of the Universe [19, 20, 21].

2.3 Production of Dark Matter

From the evidences stated in the previous section dark matter must be a stable particle, interact with gravity, and must have been produced in the early Universe. There are several mechanisms for production which can be classified as either thermal or non-thermal that allow interactions with the SM.

Thermal dark matter is produced through interactions with the plasma of the early Universe and is also in thermal equilibrium with the plasma (Figure 2.8). As the Universe ages, the temperature of the plasma decreases. This causes interactions with dark matter to slow and eventually the dark matter can no longer remain in equilibrium with the plasma. Thus, the abundance of dark matter becomes constant up to expansionary dilution.

Non-thermal dark matter is produced through other mechanisms such as out-of-equilibrium annihilations of SM particles, boson condensate formation, reheating after inflation or other phase transitions, decay of particles which may not have a thermal abundance, and many more [22, 23, 24]. Unlike thermal dark matter, non-thermal dark matter does not always need to assume a large coupling at high temperatures. For this thesis, the production of thermal dark matter in the early Universe will be covered.

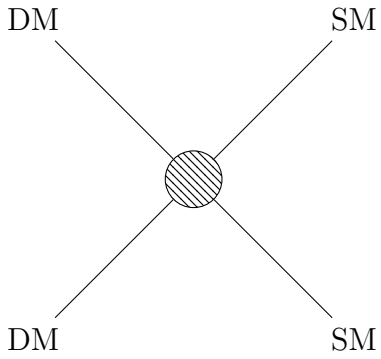

Figure 2.8: Annihilation of dark matter into SM particles occurs when looking left to right, and creation of dark matter from SM particles occurs when looking right to left. The decay process can be seen by eliminating one of the dark matter particles.

In the early Universe the number density of the particles in the plasma and the temperature were high enough for the dark matter particles to annihilate into or be created from SM particles. It is important to note that in the early Universe plasma, dark matter easily coupled to the SM particles. This is necessary so all particles in

the plasma could establish a common temperature T. The interaction of annihilation and production of dark matter particles can be described by the Boltzmann equation

$$\frac{dn}{dt} + 3Hn = \frac{1}{a^3}\frac{d(na^3)}{dt} = -\langle\sigma v\rangle(n^2 - n_{eq}^2) \tag{2.11}$$

Where n is the number density of the dark matter particles, H is the Hubble expansion given by the equation $H = \frac{1}{a}\frac{da}{dt}$, a is the cosmological scale factor, $\langle\sigma v\rangle$ is the thermally averaged annihilation rate factor, and n_{eq} is the equilibrium density of the dark matter particles. As the temperature of the primordial plasma decreases, there is not enough energy for the SM particles to create dark matter. As a result the abundance of dark matter decreases since it can still annihilate into SM particles. The number density of dark matter follows the equilibrium number density at this point and there are two limits to consider to better understand the equilibrium density, the relativistic and non-relativistic cases.

$$n_{eq} \simeq \begin{cases} T^3 & (m \ll T) \quad \text{Relativistic} \\ (mT)^{3/2}e^{-m/T} & (m \gtrsim T) \quad \text{Non-relativistic} \end{cases} \tag{2.12}$$

Both the cases describe the equilibrium number density which are dependent on the mass of dark matter and the temperature of the plasma. The dark matter density follows the equilibrium density until decoupling from the plasma.

If the dark matter particle could be held in equilibrium ($n = n_{eq}$) the abundance of the particle would decrease exponentially. However, at a certain point the number density of the dark matter particles becomes so small that there are barely any interactions. The particles can not find another particle to annihilate, and the abundance of the particles becomes constant, properly named freezing out. At this point it would be beneficial to define the variable $x = m/T$, and the point of freeze out will be when $x = x_f$, which is defined at the temperature T_f, which the dark matter decouples from SM particles.

To determine the point where freeze out occurs, Eq. 2.11 can be rewritten in terms of a new variable $Y \equiv n/s$ which is the number density of dark matter particles normalized to the entropy density s.

$$s = \frac{2\pi^2}{45}g_{*s}T^3 \tag{2.13}$$

Where g_{*s} is the number of degrees of relativistic freedom in the early Universe. This

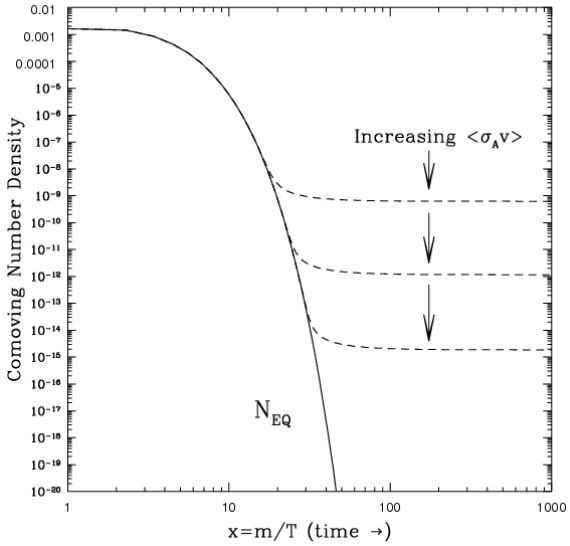

Figure 2.9: Thermal freeze out plot. The solid line is the case if $Y = Y_{eq}$, and the other three lines show different values for the annihilation rate [25].

also defines $Y_{eq} = n_{eq}/s$. The point of freeze out can help define how Y behaves when $x \lesssim x_f$, $Y \approx Y_{eq}$, and when $x \gtrsim x_f$ the abundance of dark matter can be equated to th equilibrium value at x_f, $Y(x \gtrsim x_f) = Y_{eq}(x_f)$. Rewriting Eq. 2.11

$$\frac{x}{Y_{eq}}\frac{dY}{dx} = -\frac{\Gamma s}{H}\left[(\frac{Y}{Y_{eq}})^2 - 1\right] \tag{2.14}$$

Where Γ is defined as the annihilation rate

$$\Gamma \equiv n_{eq}\langle\sigma v\rangle \tag{2.15}$$

Two regions can be examined: one where the dark matter interacts with the SM particles frequently (coupled) and the other where the dark matter no longer interacts with the SM particles (decoupled) due to the interaction rate as defined by Γ being very small.

$$\text{Coupled:} \rightarrow Y = Y_{eq} \text{ for } \frac{\Gamma}{H} \gg 1 \tag{2.16}$$

$$\text{Decoupled:} \rightarrow dY = 0 \text{ for } \frac{\Gamma}{H} \ll 1 \tag{2.17}$$

Examning Figure 2.9 the behaviour of the function can studied far away from $x = 3$. The area of interest is the region where the number density of particles in a co-moving

volume starts to deviate from the equilibrium value. This point of deviation is the freeze out point since the number density in a co-moving volume no longer changes. It can be estimated at the freeze out point that the interaction rate is equivalent to the Hubble expansion, $\Gamma(x_f) \approx H(x_f)$. Under this assumption:

$$n \sim n_{eq} \sim \left. \frac{H}{\langle \sigma v \rangle} \right|_{x_f} . \tag{2.18}$$

From this equation, it can be seen that as $\langle \sigma v \rangle$ increases the abundance of dark matter decreases, shown in Figure 2.9.

For the purpose of this thesis, only cold relics will be explored since the case where particles decouple when they are relativistic ($x_f \lesssim 3$) is not of interest. First, it would be useful to parameterize the annihilation cross section. Since the cross section is velocity dependent, and $\langle v \rangle \sim T^{1/2}$ from Kinetic Theory, it can be approximated by

$$\langle \sigma v \rangle \equiv \sum_n \sigma_n (T/m)^n = \sum_n \sigma_n x^{-n} = \sigma_0 + \sigma_1 x^{-1} + ... \tag{2.19}$$

Where the value of n corresponds to one of s-wave ($n = 0$), p-wave ($n = 1$) or a higher order wave ($n > 1$).

The solution to the Boltzmann equation can be found by the dominant cross section, given by the n$^{\text{th}}$ term, and yields the current value $Y_0 = Y_\infty$, as well as the value for x_f. The value of x_f is found to be

$$x_f \approx \ln\left[(n+1)\sqrt{\frac{90}{8\pi^3}}\frac{g}{g_*^{1/2}} m M_{Pl} \sigma_n\right] - (n+1)\ln\left(\ln\left[(n+1)\sqrt{\frac{90}{8\pi^3}}\frac{g}{g_*^{1/2}} m M_{Pl} \sigma_n\right]\right) \tag{2.20}$$

Where σ_n is the dominant cross section term described in Eq. 2.19. To find a solution now for the region where $x \gg x_f$ it can be expected that $Y \gg Y_{eq}$, thus any terms involving Y_{eq} in Eq. 2.14 can be dropped, and it becomes

$$\frac{dY}{dx} = -\lambda \sigma_n x^{-n-2} Y^2 \tag{2.21}$$

Where λ contains all constants that are independent of x. Upon integrating from x_f to $x = \infty$

$$Y_\infty = Y_0 \approx \frac{(n+1)x_f^{n+1}}{\lambda \sigma_n} \tag{2.22}$$

Knowing the current value for Y_0, the relic density can be determined

$$\rho = s_0 Y_0 m, \quad \Omega = \rho/\rho_{crit} \tag{2.23}$$

Where $s_0 \approx 3000\text{cm}^{-3}$, and $\rho_{crit} \approx (1.05h^2) \times 10^4\text{eV cm}^{-3}$ is the critical mass density, with h being the normalized Hubble parameter. The thermal relic density for a particle species χ is therefore

$$\Omega_\chi h^2 \approx (0.23 \times 10^9 \text{GeV}^{-1}) \frac{(n+1)x_f}{M_{Pl}(g_{*s}/g_*^{1/2})\langle\sigma v\rangle} \tag{2.24}$$

A leading candidate for dark matter is the weakly interacting massive particle (WIMP). This candidate interacts weakly with the SM and provide the correct thermal relic density for cold dark matter through freeze out. Measurements from the CMB, Supernovae and others agree with the ΛCDM model and observe $\Omega_{CDM}h^2 = 0.1189 \pm 0.00015$ [26, 27, 28] for the thermal relic density of cold dark matter. Using this upper bound, one can plug in $x_f \simeq 25 - 30$ and $n = 0$ into Eq. 2.24 and it can be written as

$$\Omega_\chi h^2 \simeq= 0.1 \frac{3 \times 10^{-26}\text{cm}^3/\text{s}}{\langle\sigma v\rangle}. \tag{2.25}$$

Which is astounding since the strength of a weak interaction can be found to be $\sigma v \simeq G_F^2 m_\chi^2 \simeq 3 \times 10^{-26}\text{cm}^3/\text{s}$ for $m_\chi \approx 100$ GeV, and agrees with the thermal relic density measured from experiments.

2.4 Detection of Dark Matter

Section 2.2 covered some basic evidence of dark matter and its existence and Section 2.3 explored the thermal relic abundance of dark matter present in the Universe today. These showcase how dark matter interacts with the gravitational force and that as a particle it must have an incredibly long lifetime. To fully understand dark matter some form of interaction with the SM is necessary to observe the elusive particle. However, it may be possible that dark matter connects solely to the SM through gravity which would make it incredibly difficult to detect. The three standard methods of detection are through colliders, indirect searches and direct searches. Each of the methods by themselves are powerful into probing the dark matter regime, but

all three together can place strong constraints on dark matter models.

2.4.1 Colliders

Collider experiments place limits on dark matter models, and allow high precision measurements to further constrain the models. The main method of detecting dark matter from colliders is to search for missing energy from detectors [29]. The idea comes from missing transverse momentum since if two particles collide and have their momentum in the longitudinal plane, after the collision all the transverse momentum should sum to zero. Thus, high precision is necessary in order to account for all transverse momentum in collisions.

In order to determine if the transverse momentum is missing, a trigger of visible particles is necessary. The missing momentum can be found by searching for the recoil of the dark matter particle against other particles produced. The cleanest signatures come from the scattering of a single photon (mono-photon) and scattering of a gluon (mono-jet) which both possess high transverse momentum balanced by large missing transverse momentum. These signals have been searched for at Tevatron and LHC [30, 31, 32]. The energy carried away by neutrinos in these experiments is predicted very well by the SM, so missing energy that is more than predicted can be thought of as a dark matter signal [33, 34]. However, the only way to confirm if it is in fact dark matter is through indirect or direct detection.

2.4.2 Indirect

Indirect detection searches for the products of annihilating or decaying dark matter into SM particles. This means searching for gamma rays, neutrinos, and even anti-matter such as anti-protons and positrons in regions of space with a large dark matter density. These product particles can have energies which extend up to the mass of the dark matter particle. Indirect detection is more sensitive to cosmological and astrophysical processes of dark matter annihilation and decay [35]. The flux of neutral secondary particles from annihilation follow

$$\Phi_i(\mathbf{n}, E) = \langle \sigma v \rangle \frac{dN_i}{dE} \frac{1}{8\pi m_\chi^2} \int_{l.o.s.} dl \rho_\chi^2[\mathbf{r}(l, \mathbf{n})] \tag{2.26}$$

The index i denotes the observed neutral secondary particle, l refers to the path length along the line of sight ($l.o.s.$) in the direction $\mathbf{n}$, dN_i/dE is the energy spectrum of the

observed particle, m_χ is the mass of the dark matter particle, $\rho_\chi^2[\mathbf{r}(l,\mathbf{n})]$ is the dark matter density along the line of sight, and $\langle\sigma v\rangle$ is the thermally averaged annihilation cross section of the dark matter into the observed neutral secondary particles. For charged particles, like electrons and protons, the equation is not as simple since they have non-trivial galactic propagation.

If the dark matter particle dominantly decays with lifetime τ_χ the observed flux changes to

$$\Phi_i(\mathbf{n},E) = \frac{dN_i}{dE}\frac{1}{4\pi\tau_\chi m_\chi}\int_{l.o.s.} dl\rho_\chi[\mathbf{r}(l,\mathbf{n})] \tag{2.27}$$

For dark matter masses in the sub-GeV region particles of interest include gamma rays, neutrinos, electrons, and positrons. The gamma rays and neutrinos are good probes for the indirect searches since they retain all information about their energy spectrum, and are not affected by magnetic fields due to their neutral charge. Other important information that can be obtained from the study of gamma rays and neutrinos from the annihilation or decay of dark matter is the angular distribution of the source. This may lead to a measurement of the small-scale structure of dark matter [28].

2.4.3 Direct

Direct detection is the easiest of the three methods to understand. Utilizing a detector on Earth, the experiments aim to observe a dark matter particle from the dark halo of the Milky Way scattering off of a particle. Some experiments use electron scattering [36, 37], but nuclear scatting is more common. The recoil energy off of nuclei can be described as

$$E_R = \frac{\mu^2 v^2}{m_N}(1-\cos\theta) \tag{2.28}$$

Where $\mu = m_\chi m_N/(m_\chi+m_N)$ is the reduced mass, m_χ is the mass of the dark matter particle, m_N is the mass of the nucleus, v is the incoming velocity of dark matter relative to the detector, and θ is the angle of dark matter particle after scattering [29].

For dark matter masses that are less than 1 GeV, nuclear recoil is not typically seen; however, enough energy may be deposited to interact with electrons which allows for electron ionization, excitation or molecular dissociation to occur which may be detected [38]. In this interaction some amount of energy from the dark matter particle is deposited onto the detector. These experiments are set up far below ground to help

shield the detector from cosmic rays and aim to measure the recoil energy as well as the scattering rate off the detector. The scattering rate can be calculated using the following equation [29]

$$\frac{dR}{dE}(E,t) = N_T \frac{\rho_\chi}{m_\chi} \int_{v_{min}} \frac{d\sigma}{dE}(v,E) v f_E(\overrightarrow{v},t) d^3\overrightarrow{v} \tag{2.29}$$

Where N_T is the number of target nuclei per kilogram of the detector, ρ_χ is the local dark matter density ($\rho_\chi = 0.3 GeV/cm^3$), $f_E(\overrightarrow{v},t)$ is the velocity distribution of the dark matter in the frame of the Earth, $v_{min} = \sqrt{m_N E/(2\mu^2)}$ the minimum speed of dark matter which can cause a recoil of energy detectable by a given experiment, is the dark matter-nucleus reduced mass, and $d\sigma/dE(v,E)$ is the differential cross-section for the dark matter-nucleus scattering:

$$\frac{d\sigma}{dE}(v,q) = \frac{m_N}{2\mu^2 v^2}(\sigma_{SI} F^2(q) + \sigma_{SD} S(q)) \tag{2.30}$$

Where $\sigma_{SD(SI)}$ is the spin-(in)dependent cross-section and $S(F)$ is the spin-(in)dependent nuclear form factor [29]. The full form for the nuclear form factors can be found in [39]. Constraints have been placed on WIMPs for the spin-dependent and spin-independent cases, which are summarized in Figure 2.10. Though WIMPs are a very popular candidate there are other particles that have the correct criteria for dark matter.

2.5 Dark Matter and Dark Vectors

There are a plethora of dark matter candidates and experiments that search for these elusive particles. The candidates require some extension to the SM and can fall into one or more of three categories.

The first category is hot dark matter which dictates that the particle candidate is relativistic at matter-radiation equality.

Cold dark matter is next and is defined to be non-relativistic at matter-radiation equality. Candidates of this category contain WIMPS, heavy sterile neutrinos, axions, gravitinos, Q-balls and many more. Many of these candidates have interesting phenomenology and experiments have been implemented to search for them [41, 42, 43, 44].

Warm dark matter is classified as being somewhere between relativistic and non-

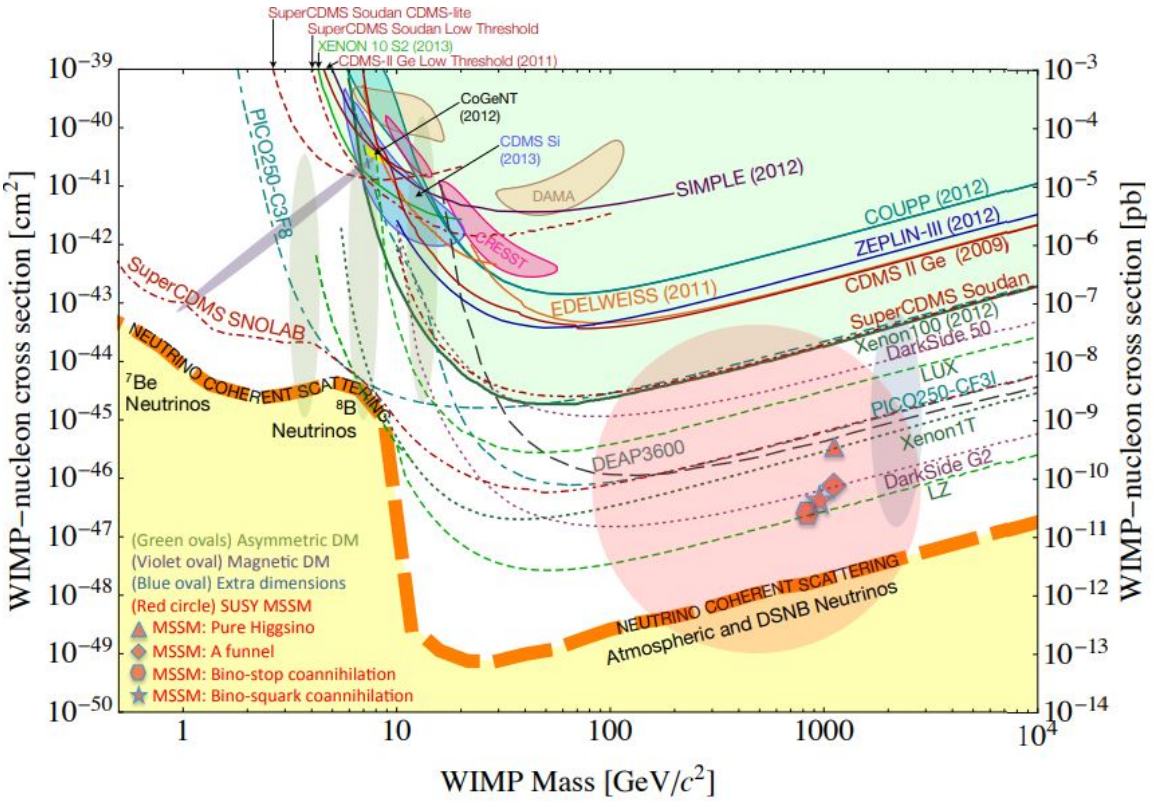

Figure 2.10: Limits placed on direct detection experiments from Oct 2013. Solid lines provide experimental data where any point above the curve is excluded, and dotted lines provide future experiments expected limits. The large orange dotted line at the bottom provides a limit where neutrinos become a significant part of the background and increase the difficulty of obtaining data. Image retrieved from [40].

relativistic at matter-radiation equality. The candidates include right-handed neutrinos, sterile neutrinos and others. The introduction of right-handed neutrinos makes sense theoretically as all other fermions in the SM have a right-handed partner. This candidate has yet to be detected but has been constrained to be either very heavy or very weakly coupled [45, 46]. Sterile neutrinos are an extension of right-handed neutrinos, however as the name implies they lack the ability to interact with the weak, strong , and EM forces.

All of these candidates can be introduced through new weakly interacting sectors of physics which extend the SM. In order to detect any candidate, a portal is required for dark matter to interact with the SM. Examples of some portals include the coupling of the photon to the axion through the dimension 5 operator $aF\tilde{F}$ [47], the right-handed neutrino coupling LHN_R, or the kinetic mixing of a new $U(1)$ vector

V_μ with hypercharge $B_{\mu\nu}V^{\mu\nu}$. These couplings were chosen as they are the lowest dimension operators that can be included and they do not currently break any rules of the SM. The next section explores the kinetic mixing of new $U(1)$ vectors that allow not only bi-linear mixing with the photon but also introduce new light vectors. [48, 49]

Chapter 3

Dark Vector Decay Widths and Energy Spectra

Dark vectors introduce a way to incorporate new forces which are coupled very weakly to the SM. It is important to note that these dark vectors may not couple to dark matter, but it is a possibility. Assuming the dark vectors can decay into SM particle, there can be cosmological impacts from these decays in the early Universe. The energy spectra and branching ratios for dark vectors are therefore important quantities to calculate and this chapter will cover new $U(1)$ gauge vector bosons with masses less than 1 GeV. The range between 1 - 2 GeV has complicated resonances due to hadrons, and for masses > 2 GeV the program `PYTHIA` [50] can be utilized. The decay channels that will be covered are e^+e^-, $\mu^+\mu^-$, $\pi^0\gamma$, $\pi^+\pi^-$ and $\pi^+\pi^-\pi^0$. Only the EM energy spectra for these channels are derived and calculated.

3.1 Dark Vector Forces

Dark forces are defined as a neutral hidden sector weakly coupled to the SM and do not interact through the known weak, strong or EM forces. Many different dark sectors could exist with their own structure, particles and force. The dark sectors of interest are new $U(1)$ vectors that use a symmetry not currently included in the SM. An effective Lagrangian that involves new dark forces is shown below, which is analogous to the photon with the addition of a mass term for the new dark vector boson.

$$\mathcal{L} = -\frac{1}{4}X_{\mu\nu}X^{\mu\nu} + \frac{1}{2}m_V^2 V_\mu V^\mu - \frac{\epsilon}{2}F_{\mu\nu}X^{\mu\nu} - g_V J_V^\mu V_\mu + \mathcal{L}_{\text{SM}} \tag{3.1}$$

Where $X_{\mu\nu} \equiv \partial_\mu V_\mu - \partial_\nu V_\mu$ is the field strength tensor of the dark vector boson, V_μ is the dark vector field, m_V is the mass of the dark vector, ϵ is the kinetic mixing strength of the dark vector, J_V^μ is the current that couples to V_μ with coupling g_V and $F_{\mu\nu}$ is the EM field strength tensor from QED. The kinetic mixing term in Eq. 3.1 can be expanded to determine how the dark vector couples to fermions from the SM.

$$\mathcal{L}_{\text{Kin.}} = -\frac{\epsilon}{2} F^{\mu\nu} X_{\mu\nu} \tag{3.2}$$

Expanding $X^{\mu\nu}$,

$$\mathcal{L}_{\text{Kin.}} = -\frac{\epsilon}{2} F^{\mu\nu} \left(\partial_\mu V_\nu - \partial_\nu V_\mu\right) \tag{3.3}$$

By using integration by parts and $F^{\mu\nu} = -F^{\nu\mu}$, it may be rewritten as

$$\mathcal{L}_{\text{Kin.}} = V_\mu \partial_\nu F^{\mu\nu} - \partial_\mu K^\mu \tag{3.4}$$

Where $K^\mu = V_\nu F^{\mu\nu}$. Using the boundary condition $\partial_\mu K^\mu = 0$ and the equation of motion $\partial_\nu F^{\mu\nu} = e J^\mu_{em}$,

$$\mathcal{L}_{\text{Kin.}} = \epsilon e V_\mu J^\mu_{\text{em}} \tag{3.5}$$

Where $J^\mu_{\text{em}} = \bar{\psi}\gamma^\mu\psi$ is the EM current, where ψ is a fermionic field. This is analogous to the photon coupling to fermions with the typical QED coupling of ϵe.

The five dark forces of interest in this paper include the kinetic mixing of a dark photon to the SM photon, $U(1)_{A'}$, the coupling to the baryon current minus the lepton current, $U(1)_{B-L}$, and the remaining three are the couplings of one lepton's current minus another lepton's current, $U(1)_{L_i - L_j}$, where $i \neq j = e, \mu, \tau$ [48]. Each of these explore a new dark force which expand the SM. The $B - L$ model is chosen since it is an non-anomalous quantity for the new force. It is also the only superposition of baryon and lepton number known to be conserved. The three lepton models are examined since there are also a non-anomalous quantity.

The new hidden $U(1)_{A'}$ force is known as the dark photon model and introduces a mediator with an unknown mass and sets $J^\mu_{A'} = 0$. These conditions allow the dark photon to only kinetically mix with the photon and can couple to other particles through the photon portal [51]. An effective gauge coupling can be determined for interactions following the field definition and Eq. 3.5

$$\alpha_{A'} = \epsilon^2 \alpha_{\text{em}} \tag{3.6}$$

where $\alpha_{\rm em} = e^2/4\pi$the EM coupling constant.

Equation 3.1 can be re-purposed for the remaining four models with the following currents.

$$J^{\mu}_{B-L} = \frac{1}{3}\bar{Q}\gamma^{\mu}Q + \frac{1}{3}\bar{u}_R\gamma^{\mu}u_R + \frac{1}{3}\bar{d}_R\gamma^{\mu}d_R - \bar{L}\gamma^{\mu}L - \bar{e}_R\gamma^{\mu}e_R; \quad U(1)_{B-L} \tag{3.7}$$

$$J^{\mu}_{L_i-L_j} = \bar{L}_{i\gamma}{}^{\mu}L_i + \bar{l}_i\gamma^{\mu}l_i - \bar{L}_j\gamma^{\mu}L_j - \bar{l}_j\gamma^{\mu}l_j \quad ; \quad U(1)_{L_i-L_j} \tag{3.8}$$

Where $i \neq j = e, \mu, \tau$. Similar to the $U(1)_{A'}$ case a gauge coupling constant can be derived for the four symmetries

$$\alpha_V = g_V^2/4\pi \tag{3.9}$$

Where $V = B-L, L_\mu - L_e, L_e - L_\tau,$ or $L_\mu - L_\tau$. The coupling to the photon is highly suppressed due to the direct coupling of the dark vectors to the baryonic and leptonic currents.

The hadronic decays that will appear for the A' and $B-L$ models have the dark vector kinetically mix with either the ρ or ω meson. To ensure that the proper coupling of the vector boson to the mesons for these channels is achieved a vector meson dominance (VMD) picture is applied. This treats the ρ and ω mesons as gauge bosons for the decays. Following [52, 53], the two mesons can be described by the generators of $U(3)$.

$$\mathbf{T}_\rho = \frac{1}{2}\boldsymbol{\lambda}_3, \quad \mathbf{T}_\omega = \frac{1}{3}\mathbb{I}_{3\times3} + \frac{1}{2\sqrt{3}}\boldsymbol{\lambda}_8 \tag{3.10}$$

Where $\boldsymbol{\lambda}_i$ are the Gell-Mann matricies and $\mathbb{I}_{3\times3}$ is the identity matrix. Upon expanding

$$\mathbf{T}_A = \text{diag}(1/2, \pm1/2, 0), \quad A = \omega, \rho \tag{3.11}$$

This can be reduced to a hidden local $U(2)$ symmetry since the two mesons are comprised of only up and down quarks and we are only interested in the sub-GeV region [27]. Above a GeV, the ϕ meson is required which would give a hidden local $U(3)$ symmetry. The coupling of A' to the up and down quark occurs through the EM current (the particle charge), and for $B-L$ it is coupled to the baryonic current (the baryon number). Thus, the couplings $\mathbf{Q}_{A'}$ and $\mathbf{Q}_{B-L}$ are

$$\mathbf{Q}_{A'} = \text{diag}(2/3, -1/3), \quad \mathbf{Q}_{B-L} = \text{diag}(1/3, 1/3) \tag{3.12}$$

Finally, the induced kinetic mixing [52, 53, 54] of the dark vectors with the ρ and ω

mesons can be calculated.

$$\kappa_{A,V} = 2\mathrm{tr}(\mathbf{T}_A \mathbf{Q}_V) = \begin{cases} 1 & A = \rho, V = A' \\ 1/3 & A = \omega, V = A' \\ 0 & A = \rho, V = B - L \\ 2/3 & A = \omega, V = B - L \end{cases} \tag{3.13}$$

This kinetic mixing term will be used for the hadronic channels that have the ρ or ω meson as the particle that kinetically mix with the dark vector.

3.2 Decay Widths and Branching Fractions

The models mentioned in the previous section have decay widths for their various channels and can be either calculated or retrieved from various sources [51, 52, 53, 55, 56, 57].

To begin, the decay width to fermion - anti-fermion is easily calculable following Feynman Rules:

$$\Gamma(V \to f\bar{f}) = \frac{C_f \alpha_X}{3} m_V \left(1 + 2\frac{m_f^2}{m_V^2}\right) \sqrt{1 - 4\frac{m_f^2}{m_V^2}} \tag{3.14}$$

Where $\alpha_X = \alpha_V x_f$ is dependent on which channel and model is chosen, m_f is the mass of the fermion, m_V is the mass of the vector boson that decayed and C_f follows

$$C_f = \begin{cases} 1, & l^+ l^- \\ 3, & q\bar{q} \\ 1/2, & \nu\bar{\nu} \end{cases} \tag{3.15}$$

An invisible channel can be obtained by examining the three generations of neutrinos, which are assumed to be Majorana particles for this thesis. The A' dark photon can decay to neutrinos through the Z boson, but the effective mixing of the light dark photon highly suppresses the channel allowing the decay width to be safely set to zero. For the $B - L$ model, the invisible channel encompasses all three generations

and the decay width is calculated to be

$$\Gamma_{\text{inv}} = 3 \cdot \Gamma(V \to \nu\bar{\nu}) = \frac{\alpha_X}{2} m_V \tag{3.16}$$

The same is true for the lepton models, but the factor of 3 is replaced with 2 since only two generations of neutrinos are not highly suppressed. For completeness, the decay widths to e^+e^- and $\mu^+\mu^-$ are found by substituting in the mass of the electron or muon into Eq. 3.14.

In the sub-GeV region, there are three hadronic channels that have resonances around the mass of the ρ or ω meson. The channels are $\pi^0\gamma$, $\pi^+\pi^-$ and $\pi^+\pi^-\pi^0$ can also be found analytically. The decays widths were calculated using VMD as done in [52, 53]. The first of the decays was calculated to be

$$\Gamma(V \to \pi^0\gamma) = \kappa^2_{\omega,V} \frac{3\alpha_V}{128\pi^3} \frac{m_V^3 \alpha_{\text{em}}}{f_\pi^2} \left(1 - \frac{m_\pi^2}{m_V^2}\right)^3 \left|F_\omega(m_V^2)\right|^2 \tag{3.17}$$

Where $f_\pi \simeq 93\text{MeV}$ is the pion decay constant and $F_\omega(m_V^2) \simeq (1 - s/m_\omega^2 + i\Gamma_\omega/m_\omega)^{-1}$ is the Breit-Wigner form factor due to the ω meson being a propagator in this decay.

To determine the decay width of $\pi^+\pi^-$ in the $U(1)_{A'}$ model different methods were explored. The first method was to use the decay width calculated in [53]

$$\Gamma(V \to \pi^+\pi^-) = \kappa^2_{\rho,V} \frac{\alpha_V m_V}{12} \left(1 - 4\frac{m_\pi^2}{m_V^2}\right)^{3/2} \left|F_\pi(m_V^2)\right|^2 \tag{3.18}$$

$$F_\pi(m_V^2) = F_\rho(m_V^2)\Big[1 + \frac{1+\delta}{3} \frac{\tilde{\Pi}_{\rho\omega}(m_V^2)}{m_V^2 - m_\omega^2 + i m_\omega \Gamma_\omega}\Big] \tag{3.19}$$

Where F_ρ is the familiar Breit-Wigner form factor for the ρ meson as a propagator, $\delta = 2g_x/\varepsilon e$, and $\tilde{\Pi}_{\rho\omega}$ is the $\rho - \omega$ mixing parameter which has been experimentally determined to be $\tilde{\Pi}_{\rho\omega}(m_V^2 = m_\omega^2) = -3500 \pm 300\ \text{MeV}^2$ [53, 58]. The mixing parameter is not known at other masses, and as such the mixing parameter was set to the ansatz $\tilde{\Pi}_{\rho\omega}(m_V^2) = \tilde{\Pi}_{\rho\omega}(m_\omega^2)\frac{m_V^2}{m_\omega^2}$ since it is expected to vanish when $m_V \to 0$ [53]. This was found to not be a reliable computation and a more solid approach was necessary.

For the second method experimental evidence was utilized instead of theoretical predictions. From [55], the decay width for $A' \to \pi^+\pi^-$ was explored.

$$\Gamma_{A' \to \pi^+\pi^-} = \Gamma_{A' \to \mu^+\mu^-} \mathcal{R}_\mu^{\pi^+\pi^-}(m_{A'}^2) \tag{3.20}$$

Where $\Gamma_{A'\to\mu^+\mu^-}$ is defined in Eq. 3.14 with $m_f = m_\mu$ and $\mathcal{R}_\mu^{\pi^+\pi^-} \equiv \sigma(e^+e^- \to \pi^+\pi^-)/\sigma(e^+e^- \to \mu^+\mu^-)$ is determined experimentally and can be extracted from BaBar data [59]. This is a more reliable method of determining the channel as the measured results of $\mathcal{R}_\mu^{\pi^+\pi^-}$ encompasses the $\rho-\omega$ mixing parameter. This method of extracting data was tested against the $\pi^+\pi^-\pi^0$ channel and showed promising results, gaining confidence that this method works.

The final decay channel is the most complicated and the results have been calculated and obtained from [52, 53]

$$\Gamma(V \to \pi^+\pi^-\pi^0) = \kappa_{\omega,V}^2 \frac{3\alpha_V}{16\pi^4}\left(\frac{g_{\rho\pi\pi}^2}{4\pi}\right)^2 \frac{m_V}{f_\pi^2}\mathcal{I}(m_V^2)\left|F_\omega(m_V^2)\right|^2 \tag{3.21}$$

$$\begin{aligned}\mathcal{I}(m_V^2) = &\int dE_+ dE_- [|\mathbf{p}_+|^2|\mathbf{p}_-|^2 - (\mathbf{p}_+\cdot\mathbf{p}_-)^2] \\ &\times\Big|\frac{1}{m_\rho^2-(p_++p_-)^2-i\Gamma_\rho m_\rho} + \frac{1}{m_\rho^2-(p_++p_0)^2-i\Gamma_\rho m_\rho} + \\ &\frac{1}{m_\rho^2-(p_++p_0)^2-i\Gamma_\rho m_\rho}\Big|^2\end{aligned} \tag{3.22}$$

Where $g_{\rho\pi\pi}$ is the $\rho\pi\pi$ coupling fixed by $g_{\rho\pi\pi}^2/4\pi \approx 3.0$ observed by the decay $\rho \to \pi\pi$. $\mathcal{I}(m_V^2)$ is the integral over phase space of the energy of the charged and neutral pions where, $p_\pm = (E_\pm, \mathbf{p}_\pm)$ and $p_0 = (E_0, \mathbf{p}_0)$ are the momenta for the charged pions and the neutral pion in the rest frame of the V particle. The bounds for the integral in $\mathcal{I}(m_V^2)$:

$$m_\pi \le E_+ \le \frac{m_V^2 - 3m_\pi^2}{2m_V} \tag{3.23}$$

$$b_\pm = \frac{1}{2}\Big(m_V - E_+ \pm |\mathbf{p}_+|\sqrt{\frac{m_V^2-2E_+m_V-3m_\pi^2}{m_V^2-2E_+m_V+m_\pi^2}}\Big), \quad b_- \le E_- \le b_+ \tag{3.24}$$

The branching fraction of the decays in the sub-GeV region can then be calculated by using the formula:

$$\mathrm{Br}_c = \frac{\Gamma_c}{\Gamma_T} \tag{3.25}$$

Where Br_c is the probability of the particle to decay to a channel c, Γ_c is the decay width of the channel in question and Γ_T is the total decay width of the particle and follows the formula $\Gamma_T = \sum_i \Gamma_i$. Branching ratios for the various models are in Figures 3.1 and 3.2. The hadronic components and the lepton not included in the current for the $L_i - L_j$ models were extracted from [51] for Figure 3.2. In all of the

models the branching ratios for those channels were $< (1\%)$ and were safely neglected when calculating their contributions.

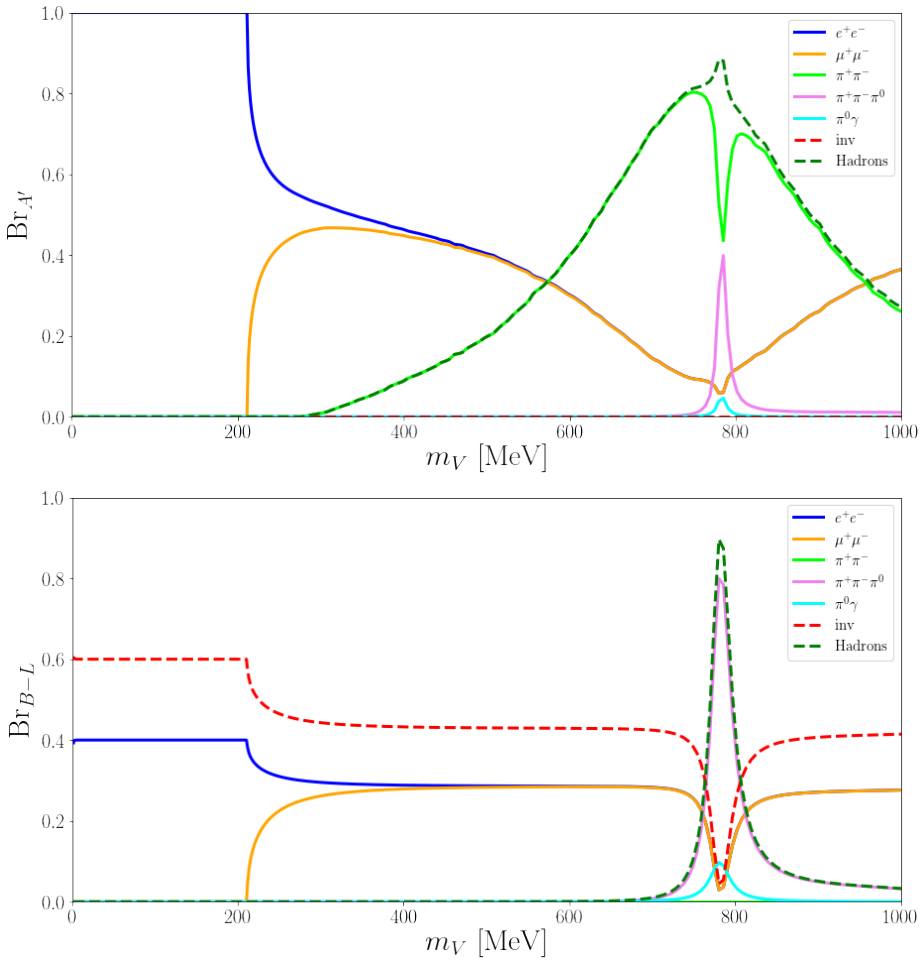

Figure 3.1: The branching fraction for the $U(1)_{A'}$ (top) and $U(1)_{B-L}$ (bottom) models. The hadron line (dotted green line) corresponds to the sum of $\pi^+\pi^-$ (solid green), $\pi^+\pi^-\pi^0$ (solid pink) and $\pi^0\gamma$ (solid light blue).

3.3 Energy Distributions in Different Frame

To determine the effects of EM energy injection into the early Universe, we want the energies of the vector boson decay products in the vector rest frame. Since we want EM energy, we require that the decay products be electrons and photons. For muons and pions, which decay into electrons, photons, and neutrinos, we need to boost the energy of the electrons and photons from the muon or pion rest frame into the vector

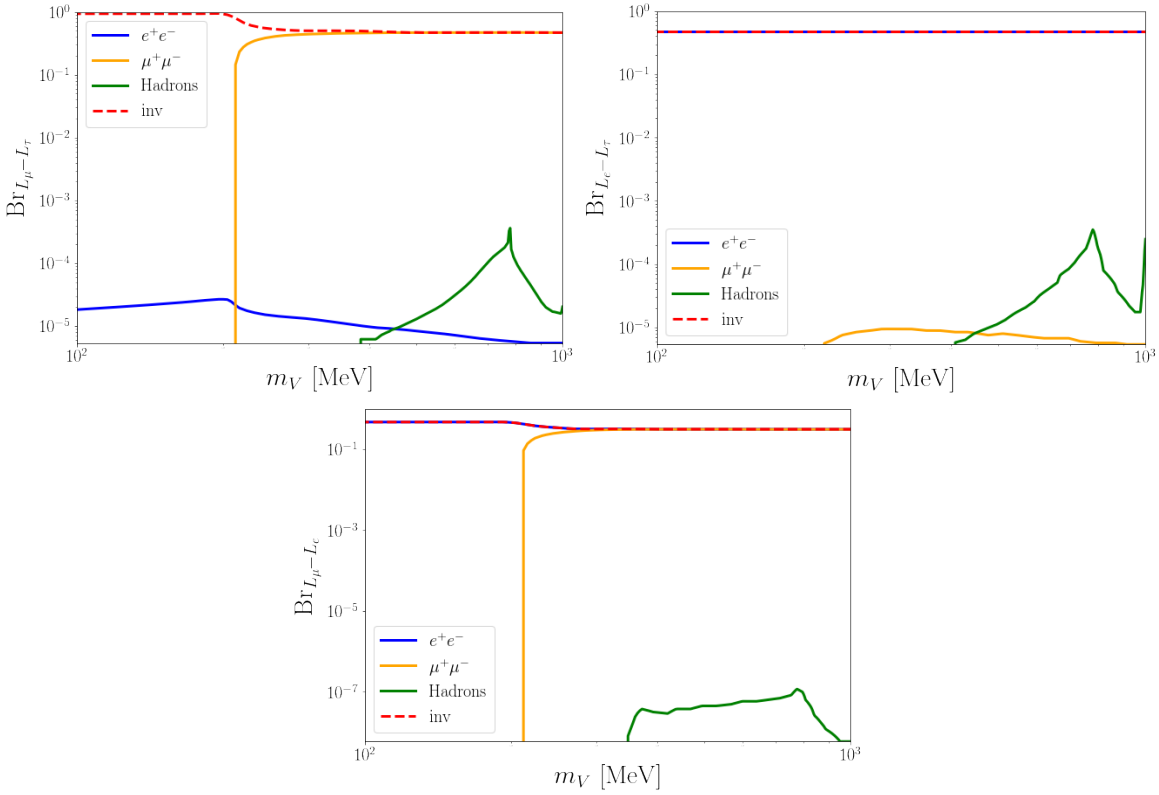

Figure 3.2: The branching ratios for the lepton models. $L_\mu - L_\tau$ model (upper left), $L_e - L_\tau$ model (upper right), $L_\mu - L_e$ model (bottom). For $L_e - L_\tau$ and $L_\mu - L_e$, the e^+e^- channel (solid blue line) is hidden behind the invisible neutrino channel (solid red line).

boson rest frame. This section gives a brief overview of how to change frames.

For a decay process that has an energy and angular distribution $p(E, \Omega)$ in the decay rest frame, E is energy of the product, and Ω refers to the direction relative to some arbitrary axis. This probability must be normalized such that

$$\int dE \int d\Omega p(E, \Omega) = 1 \tag{3.26}$$

This can be marginalized to find the distribution of the energy

$$f(E) \equiv \int d\Omega p(E, \Omega) \tag{3.27}$$

In order to find the energy distribution of the decay product in a frame that is boosted by some value for $\beta \geq 0$, the energy (E) and momentum (p) of the decay product

must be boosted. Without loss of generality, one can choose to boost the momentum along the z-axis

$$E' = \gamma(E + \beta p\cos\theta), \quad p'_z = \gamma(p\cos\theta + \beta E), \quad p'_x = p_x, \quad p'_y = p_y \tag{3.28}$$

Where $\cos\theta$ is the angle between the momentum and the z-axis and the values for γ and β are dependent on the mass (m_d) and energy (E_d) of the particle that decayed.

$$\gamma = \frac{E_d}{m_d}, \quad \beta = \frac{\sqrt{\gamma^2 - 1}}{\gamma} \tag{3.29}$$

From here the probability distribution can be found by changing the variables to the boosted frame.

$$1 = \int dE \int d\Omega p(E,\Omega) = \int dE' \left[\int d\Omega \left| \frac{\partial(E',\Omega)}{\partial(E,\Omega)} \right|^{-1} p(E',\Omega) \right] \tag{3.30}$$

Where the Jacobian factor can easily be calculated

$$\left| \frac{\partial(E',\Omega)}{\partial(E,\Omega)} \right| = \gamma\left(1 + \frac{E}{p}\cos\theta\right) \tag{3.31}$$

The term in the square brackets in Eq. 3.30 is the new $\tilde{f}(E')$ for the boosted E'.

$$\tilde{f}(E') = \int d\Omega \left(\gamma \left(1 + \frac{E}{p}\cos\theta \right) \right)^{-1} p(E',\Omega) \tag{3.32}$$

This technique can be applied to the the decay of V if electrons or photons are not the initial product of the decay.

3.4 $V \to e^+e^-$

The decay to e^+e^- is trivial and the spectra is easily calculable. The energy distribution of the electron and positron must be $m_V/2$ in the rest frame of V.

$$\left. \frac{dN_{e^\pm}}{dE} \right|_V = \delta\left(E_{e^\pm} - \frac{m_V}{2}\right) \tag{3.33}$$

Both the electron and positron have the same distribution in this decay and no boost is necessary since the electron and positron are immediately present when V decays. The sum of the electron and positron energy spectra is therefore

$$\left.\frac{dN_e}{dE}\right|_V = \left.\frac{dN_{e^+}}{dE}\right|_V + \left.\frac{dN_{e^-}}{dE}\right|_V = 2\delta\left(E_e - \frac{m_V}{2}\right) \tag{3.34}$$

Additional photons are produced from final state radiation (FSR) of the electrons, but are non-leading terms. In fact, each decay channel has some FSR term and are all handled properly in the analysis.

As a side note, the invisible channel follows almost the exact same treatment as the electrons. The total energy spectra of the neutrinos the same as Eq. 3.34, replacing e and $e^{\pm}$ with ν. The factor of two is present in this case since there are two neutrinos as the final products of decay.

3.5 $V \to \pi^0\gamma$

The initial photon emitted at the beginning is the simplest to solve for since it is mono-energetic and is a delta spike which requires no boost.

$$\left.\frac{dN_\gamma}{dE}\right|_V = \delta\left(E_\gamma - \frac{m_V}{2}\left(1 - \frac{m_\pi^2}{m_V^2}\right)\right) \tag{3.35}$$

The complication comes from the neutral pion decay, which almost always decays to two photons [27]. The energy distribution of the photons can be obtained from examining the pion's rest frame and boosting the results to the rest frame of V. The first step is to notice that in the decay rest frame of the pion, both photons are mono-energetic, $E_o = m_\pi/2$, and emitted at angles such that the difference is 180° (Figure 3.3). Thus, the energy distribution of the two photons in the pion's rest frame is

$$\left.\frac{dN_\gamma}{dE}\right|_{\pi^0} = 2\delta(E_\gamma - E_o) \tag{3.36}$$

The factor of 2 is present due to 2 photons produced from the decay of the pion. This must be boosted into the V rest frame to produce the desired photon spectra.

In this frame only one boost must be applied to be in the V rest frame and must

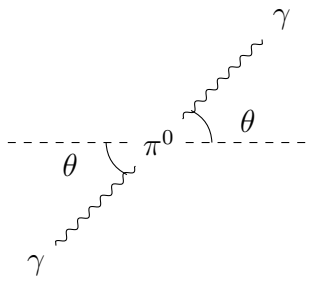

Figure 3.3: Decay of the $\pi^0 \to \gamma\gamma$ in the pion rest frame. The two photons in this frame are emitted the same energy and at the angle θ relative to some arbitrary axis.

use the energy and mass of pion to calculate the values of γ and β from Eq. 3.29. It can also be noted that the boosted energy, E', in Eq. 3.28 can be simplified due to the photon being massless.

$$E' = \gamma E_o(1 + \beta \cos\theta) \tag{3.37}$$

If boosted along the positive z-axis, the two photons emitted will have different energies depending on the decay angle relative to the positive z-axis. The photon with the angle which is more along the positive z-axis, $\cos(\theta)$, will have a greater energy than the other photon who will have a relative decay angle of $\cos(\theta + 180°) = -\cos(\theta)$, thus the two photons transform under the boost as

$$E'_{\pm} = \gamma E_o(1 \pm \beta \cos\theta) \tag{3.38}$$

Where + is the photon that in more aligned with the positive z-axis, and the - is for the other photon. It should be noted that because θ is the decay angle of the photon more aligned along the positive z-axis, it restricts the value of $\cos\theta \in [0, 1]$. Eq. 3.36, can be expanded to demonstrate the effect the boost will have on the two photons.

$$\left.\frac{dN_\gamma}{dE}\right|_{\pi^0} = \delta(E_\gamma - E_o) + \delta(E_\gamma - E_o) \tag{3.39}$$

When boosted to the V rest frame, using $\gamma = \dfrac{E_\pi}{m_\pi} = \dfrac{m_V}{2m_\pi}(1 + \dfrac{m_\pi^2}{m_V^2})$

$$\begin{aligned}\left.\frac{dN_\gamma}{dE}\right|_V &= \int_0^1 dx \frac{1}{\gamma(1+\beta x)}\delta\left(\frac{E'}{1+\beta x} - E_o\right) + \frac{1}{\gamma(1-\beta x)}\delta\left(\frac{E'}{1-\beta x} - E_o\right) \\ &= \left.\frac{dN_\gamma}{dE}_+\right|_V + \left.\frac{dN_\gamma}{dE}_-\right|_V\end{aligned} \tag{3.40}$$

Where $x = \cos\theta$. This can be solved analytically for the two cases resulting in the total photon injection due to the pion decay.

$$\left.\frac{dN_\gamma}{dE}_+\right|_V = \begin{cases} \frac{1}{\beta\gamma}\frac{1}{E_o} & : \quad \gamma \leq \frac{E'}{E_o} \leq \gamma(1+\beta) \\ 0 & : \quad \text{otherwise} \end{cases} \tag{3.41}$$

$$\left.\frac{dN_\gamma}{dE}_-\right|_V = \begin{cases} \frac{1}{\beta\gamma}\frac{1}{E_o} & : \quad \gamma(1-\beta) \leq \frac{E'}{E_o} \leq \gamma \\ 0 & : \quad \text{otherwise} \end{cases} \tag{3.42}$$

Or for the total photon injection:

$$\left.\frac{dN_\gamma}{dE}\right|_V = \begin{cases} \frac{1}{\beta\gamma}\frac{1}{E_o} & : \quad \gamma(1-\beta) \leq \frac{E'}{E_o} \leq \gamma(1+\beta) \\ 0 & : \quad \text{otherwise} \end{cases} \tag{3.43}$$

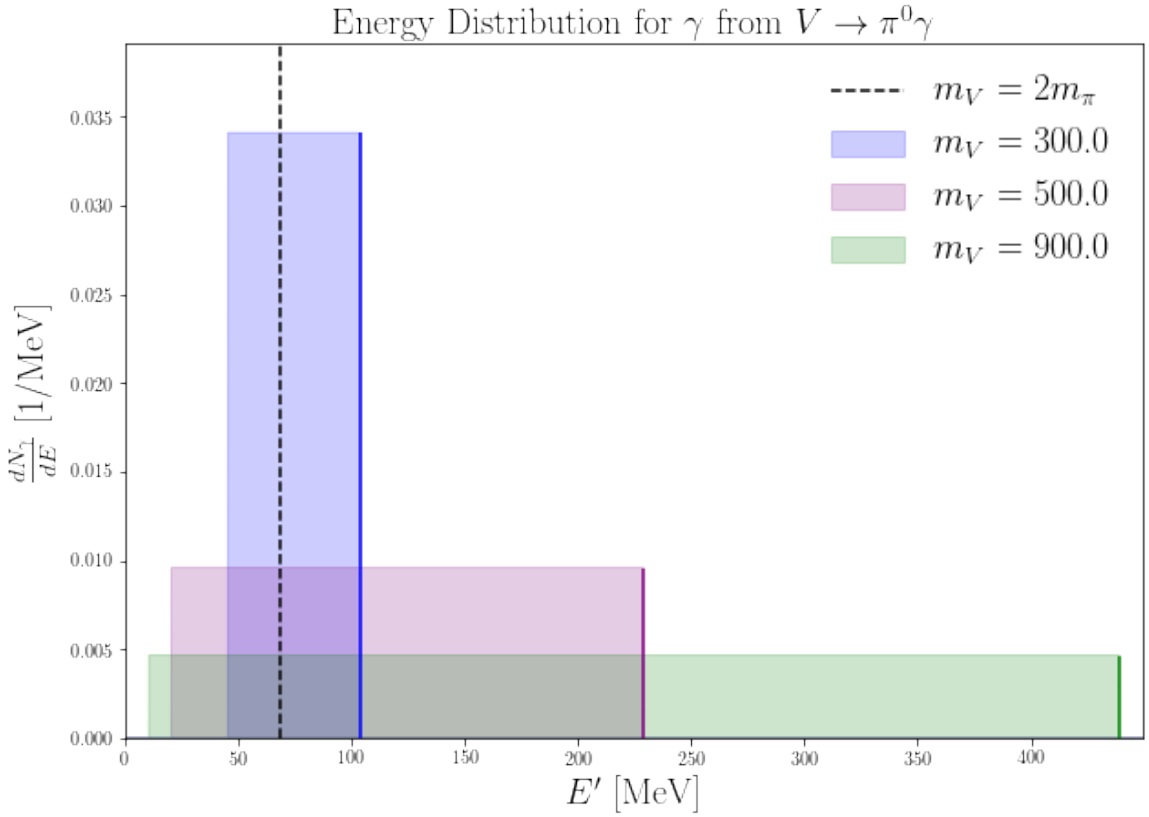

Figure 3.4: Photon energy distribution in the V rest frame. The total photon energy distribution for various masses of V. The coloured line on the right edge of the boxes is the energy of the initial photon emitted from the decay.

3.6 $V \to \mu^+\mu^-$

This channel requires a bit more care as the electron and positron energy distributions are not as trivial as the previous sections. The muon and anti-muon decays are shown in Figure 3.5.

The final state electron from the three body decay is a Michel electron [27] and yields a non-trivial distribution when examined in the muon rest frame. The distribution can be described by

$$f(y) = 2y^2\Big[(3-2y) + P(1-2y)\cos\theta\Big]\Theta(1-y) \tag{3.44}$$

Where $y = E_{e^-}/E_{max}$ with $E_{max} = m_\mu/2$ being the maximum energy of the electron in the muon rest frame, $P \in [-1, 1]$ is the net polarization of the muon (which for simplicity can be oriented along the z-axis), $\cos\theta$ is the electron angle relative to the

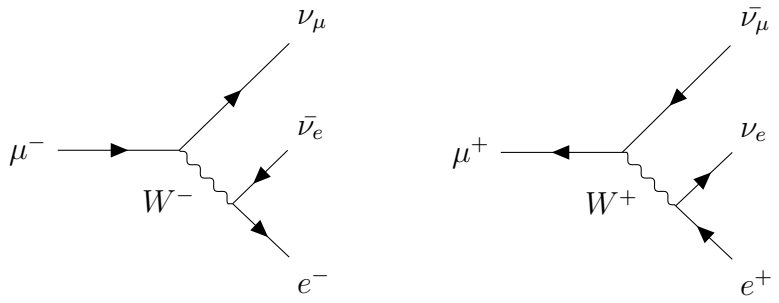

Figure 3.5: Decays of muon and antimuon via the Weak force since the muon changes lepton flavour.

polarization axis, and $\Theta(x)$ is the Heaviside step function defined as

$$\Theta(x) = \begin{cases} 0 & x < 0 \\ 1 & x \leq 0 \end{cases} \tag{3.45}$$

It is important to note that the sign of the polarization term flips when working with the antimuon. The energy distribution in the rest frame of the muon is Eq. 3.44

$$\left.\frac{dN_{e^-}}{dE}\right|_{\mu^-} = \frac{f(y)}{E_{max}} \tag{3.46}$$

This is not the energy distribution in the V rest frame and a boost must be applied in order to achieve the desired result. Only a single boost factor must be used where $\gamma = \frac{E_\mu}{m_\mu} = \frac{m_V}{2m_\mu}$, which when combined with Eq.'s 3.28, 3.29, and 3.30 results in the updated energy distribution in the V rest frame.

$$\begin{aligned}\left.\frac{dN_{e^-}}{dE}\right|_V =& \frac{1}{E_{max}} \int_{-1}^{+1} dx \frac{y'^2}{(\gamma(1+\beta x))^3} \left[3 - \frac{2y'}{\gamma(1+\beta x)}\right] \Theta\left(1 - \frac{y'}{\gamma(1+\beta x)}\right) \\ &+ \frac{P}{E_{max}} \int_{-1}^{+1} dx \frac{xy'^2}{(\gamma(1+\beta x))^3} \left[1 - \frac{2y'}{\gamma(1+\beta x)}\right] \Theta\left(1 - \frac{y'}{\gamma(1+\beta x)}\right)\end{aligned} \tag{3.47}$$

Where the electron is effectively massless under the assumption that $m_V \gg m_e$, $x = \cos\theta$, and $y' = y\gamma(1+\beta x)$ is in the V rest frame as required.

The electron and positron equally contribute to the energy spectra and their

contributions can be summed together to give the total electron energy.

$$\left.\frac{dN_e}{dE}\right|_V = \left.\frac{dN_{e^-}}{dE}\right|_V + \left.\frac{dN_{e^+}}{dE}\right|_V \tag{3.48}$$

By summing the two together the polarization term disappears because the positron has the same form but with the sign of P negated. This makes sense because in vector decays there are as many up polarizations as there are down ones provided that the initial vector is unpolarized.

The total energy spectrum for e, the sum of electrons and positrons, can be found analytically by solving the first term in Eq. 3.47 yielding the energy distribution

$$\left.\frac{dN_e}{dE}\right|_V = \frac{2}{E_{max}} \begin{cases} 0 & : \quad y' > \sqrt{\frac{1+\beta}{1-\beta}} \\ \frac{2y'^2}{\gamma}\left[\frac{3}{1-\beta^2} - 2y'\frac{1+\beta^2/3}{(1-\beta^2)^3/2}\right] & : \quad y' < \sqrt{\frac{1-\beta}{1+\beta}} \\ \frac{1}{\beta\gamma}\left(\frac{3}{2}\left(1 - y'^2\frac{1-\beta}{1+\beta}\right) - \frac{2}{3}\left[1 - y'^3\left(\frac{1-\beta}{1+\beta}\right)^{3/2}\right]\right) & : \quad \sqrt{\frac{1-\beta}{1+\beta}} < y' < \sqrt{\frac{1+\beta}{1-\beta}} \end{cases} \tag{3.49}$$

3.7 $V \to \pi^+\pi^-$

This decay channel behaves almost identically to the previous channel, with some slight changes. The first change is that the net polarization of the muon depends if it decays from a positively or negatively charged pion. The second change is that there will be two boosts needed to achieve the final spectra of the electrons since the charged pion decays almost exclusively to muons, with a maximum energy transfer of $E_{max} = m_\pi/2$, and the resulting muons decay into electrons or positrons.

The net polarization of the muons can be found by examining each pion. For the π^+ decay to an antimuon and muon neutrino there is a net spin of 0, since the pion is a spinless particle. The neutrino is by definition a left-handed particle which means that its spin angular momenta points in the opposite direction of its linear momenta. Therefore, in order to have a net spin of zero in the decay, the antimuon must have its spin angular momentum pointed exactly backward along its momenta. Therefore, if the polarization is aligned along the axis the antimuon is travelling along, the net polarization for the antimuon is -1. A similar treatment can be done for the muon, resulting in a polarization of +1.

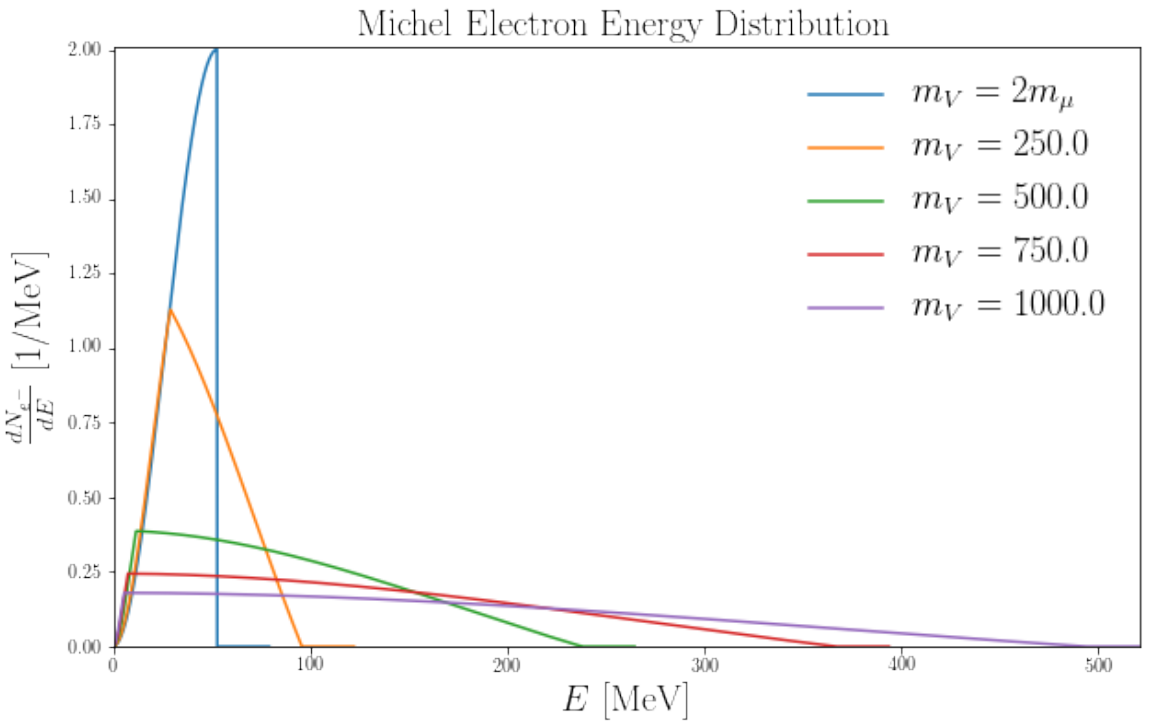

Figure 3.6: Two masses of V are shown to demonstrate the effect that the mass and polarization have on the energy spectrum of the electron. For a mass that is equal to $2m_\mu$, no polarization effects appear.

Knowing the polarization, the energy spectra for the electron is

$$\left.\frac{dN_{e^-}}{dE}\right|_{\mu^-} = \frac{f(y)}{E_{max}} \tag{3.50}$$

Where $f(y)$ is Eq. 3.44. A $\bar{\gamma}$ factor can be computed for the decay of $V \to \pi^+\pi^-$.

$$\bar{\gamma} = \frac{E_\pi}{m_\pi} = \frac{m_V}{2m_\pi}, \quad \bar{\beta} = \frac{\sqrt{\bar{\gamma}^2 - 1}}{\bar{\gamma}} \tag{3.51}$$

The energy and momentum of the muon in the pion's rest frame are also necessary.

$$E_{\mu^-} = \frac{m_\mu}{2}\left(1 + \frac{m_\mu^2}{m_\pi^2}\right), \quad p_{\mu^-} = \frac{m_\mu}{2}\left(1 - \frac{m_\mu^2}{m_\pi^2}\right) \tag{3.52}$$

A new angle, $\cos\alpha$, can be defined to be the polar angle of the muon relative to the boost direction of the pion in the pion rest frame. The angle $\cos\theta$s is the angle between the electron momentum and the muon polarization in the muon rest frame.

The z-axis can be chosen as the direction for the emitted muon without loss of generality, which also aligns with the muon polarization axis. The values for γ and β can be calculated for the emitted muon.

$$\gamma = \left(\frac{m_\pi}{2m_\mu}\right)\left(1 + \frac{m_\mu^2}{m_\pi^2}\right), \quad \beta = \frac{\sqrt{\gamma^2 - 1}}{\gamma} \tag{3.53}$$

This however is not the required frame since V is not at rest, so it must be boosted to the pion rest frame. Since the muon-electron system implicitly lies in the x-z plane by the choices made earlier, other boosts must be considered in an arbitrary direction $\hat{n}$, which is the direction in which the pion is emitted from V. This leaves new values $\overline{\gamma}$ and $\overline{\beta}$ as the boosts necessary to be in the V rest frame. The new boosted frame is:

$$E'' = E'\overline{\gamma}[1 + \overline{\beta}(\hat{p_e}' \cdot \hat{n})]. \tag{3.54}$$

Where E' is the energy of the electron in the pion rest frame given by Eq. 3.37, with the new values for γ and β as defined in Eq. 3.53, with $E_o = m_\mu/2$. The two other variable in the equation are $\hat{p_e}'$, the unit vector in the direction of the electron momentum in the V rest frame, and $\hat{n}$ is the pion boost direction in the lab frame. The value for $\hat{n}$ can be set to $\hat{n} = (\sin\alpha\cos\phi, \sin\alpha\sin\phi, \cos\alpha)$, which results in the dot product

$$\hat{p_e}' \cdot \hat{n} = \sin\alpha\cos\phi\sin\theta' + \cos\alpha\cos\theta` \tag{3.55}$$

$$\cos\theta' = \frac{\cos\theta + \beta}{1 + \beta\cos\theta} \tag{3.56}$$

The final result of combining everything together gives the lab frame electron energy as a function of the particle masses and the independent variables $y \in [0,1]$, $x \equiv \cos\theta \in [-1,1]$, $z \equiv \cos\alpha \in [-1,1]$, and $\phi \in [0, 2\pi]$. These four variables are all uniformly distributed over the specified ranges.

$$\left.\frac{dN_{e^-}}{dE}\right|_V = \frac{1}{2} \times \frac{1}{2} \times \frac{1}{2\pi} \int dz \int dx \int d\phi \left|\frac{\partial(E'', z, x, \phi)}{\partial(E, z, x, \phi)}\right|^{-1} \left(\left.\frac{dN_{e^-}}{dE''}\right|_{\mu^-}\right) \tag{3.57}$$

This is a complicated integral to solve, and a Monte Carlo method can be used to find the distribution of the electrons and positrons.

An interesting feature about this decay is the polarization. It is set to $P = +1$ for

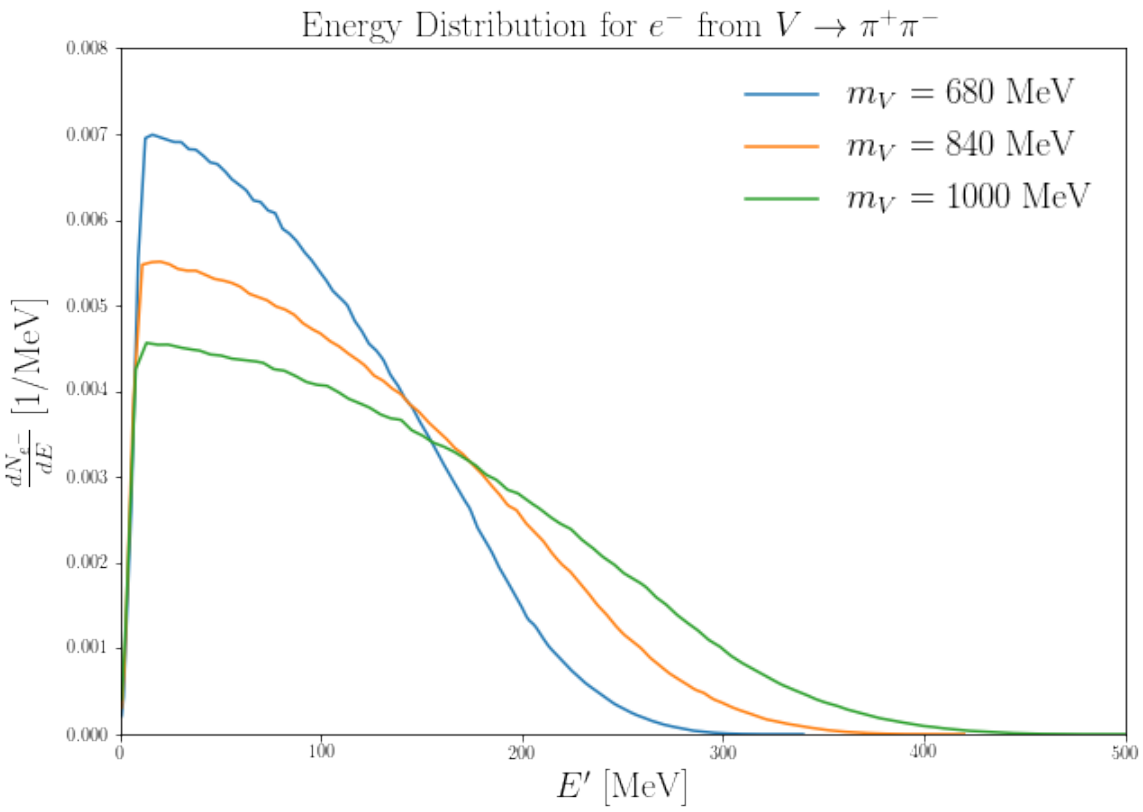

Figure 3.7: Electron energy distribution for $V \to \pi^+\pi^-$.

the muon decay, and as such the sign in front of P is left untouched. When examining the charge conjugate mode, the positron spectra, the sign in front of the P is negated, and $P = -1$, so the electron energy spectrum in Eq. 3.57 is also the energy spectrum for the positron. Thus, the total electron energy spectra is

$$\left.\frac{dN_e}{dE}\right|_V = 2\left.\frac{dN_{e^-}}{dE}\right|_V \tag{3.58}$$

3.8 $V \to \pi^+\pi^-\pi^0$

This channel follows the $V \to \pi^+\pi^-$ channel closely but instead of mono-energetic pions there is an energy distribution for the three pions. The final energy spectra are similar to Eq.'s 3.4 and 3.57, but include a term which accounts for the energy distribution of the pions.

The energy spectrum of the final state particles was found by examining the scenario of the vector boson, V, at rest and determining the energy of the pions. For

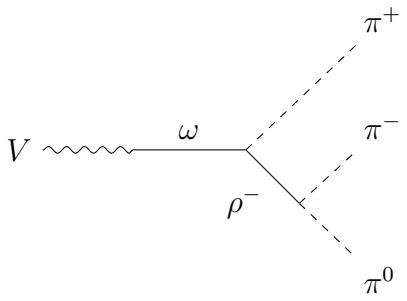

Figure 3.8: Decay of $V \to \pi^+\pi^-\pi^0$. There are two more similar decays where the difference is that π^+ switches places with π^- or π^0. To conserve the charge the ρ^- changes to ρ^+ or ρ^0 respectively.

the analysis, the pion mass was averaged to ~ 138 MeV. The distribution of energy for the pions was calculated by performing a numerical integration of Eq. 3.21 and plotting $\frac{1}{\Gamma}\frac{d^2\Gamma}{dE_+ dE_-}$ for E_- against E_+ in the bounds as stated in Eq. 3.23 and Eq. 3.24. The results are shown in Figure 3.9.

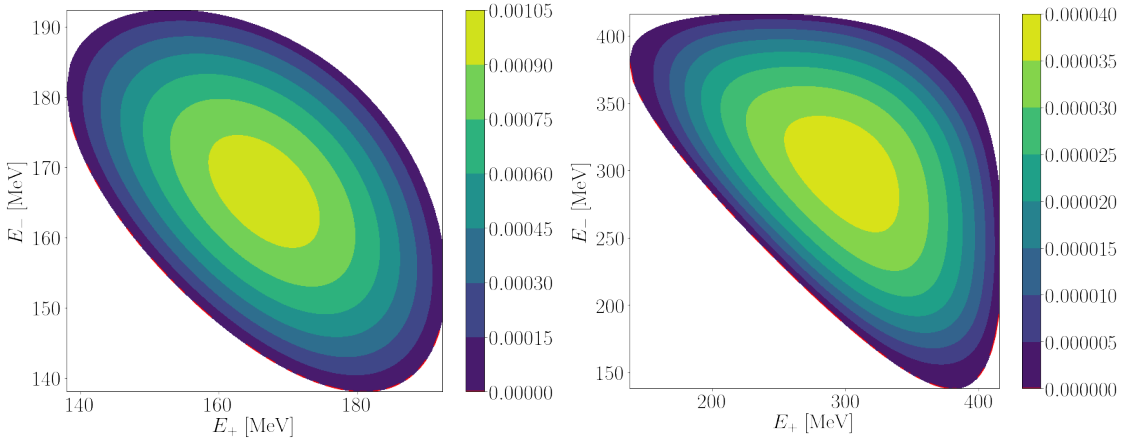

Figure 3.9: Result of calculating $\frac{1}{\Gamma}\frac{d^2\Gamma}{dE_+ dE_-}$ for $m_V = 500$ MeV (left) and $m_V = 900$ MeV (right) by using Eq. 3.21.

With an understanding of what to expect from the analytical method, a Monte Carlo method was created for further analysis. The Monte Carlo method generated random uniform values of E_+ and E_- between the bounds given in Eq. 3.23. The energy of the last pion could also be determined from conservation of energy, $E_0 = m_V - E_- - E_+$. Weights could be generated from Eq. 3.22, and 2D plots were generated for the different pion energies. As expected, the Monte Carlo method (Figure 3.10) was not only faster to compute yielding the same results as the analytical method, but it was able to generate 1D histograms of the energy and momentum

distributions for the pions (Figures 3.11 and 3.12).

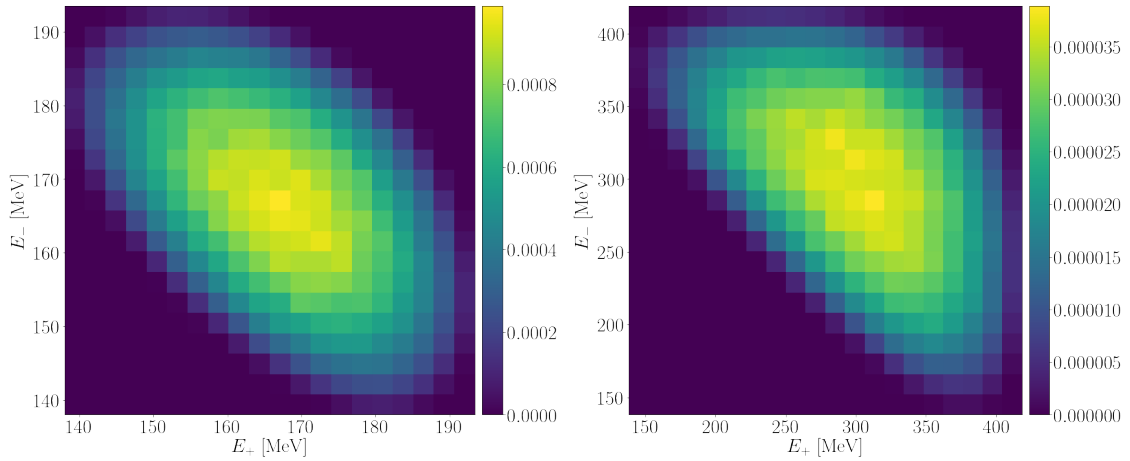

Figure 3.10: Result of calculating $\frac{1}{\Gamma}\frac{d^2\Gamma}{dE_+ dE_-}$ with the Monte Carlo method for $m_V = 500$ MeV (left) and $m_V = 900$ MeV (right) by using Eq. 3.21.

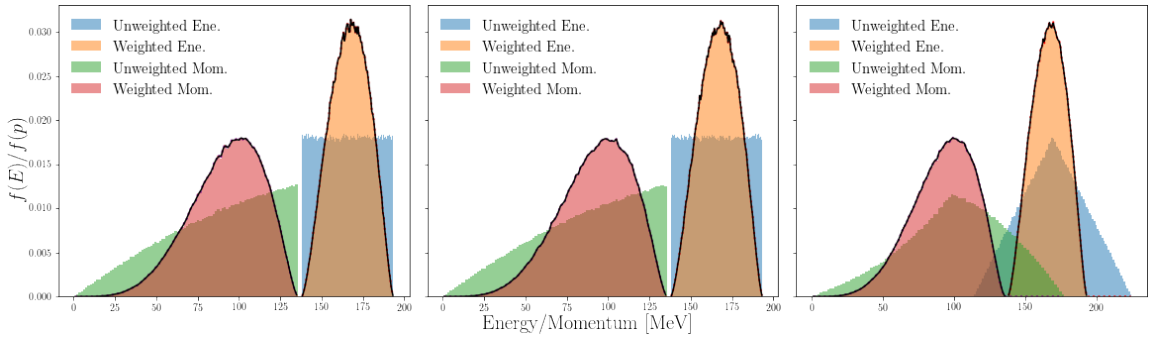

Figure 3.11: 1D histogram of each pion energy for $m_V = 500$ MeV from the Monte Carlo method.

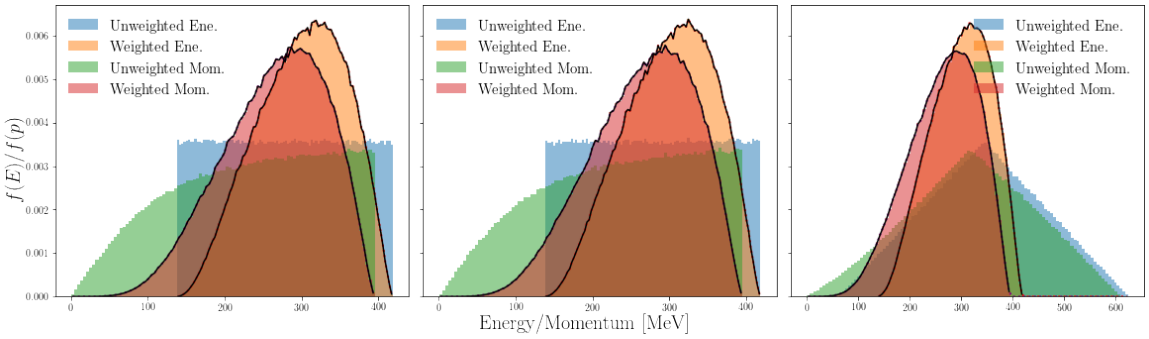

Figure 3.12: 1D histogram of each pion energy for $m_V = 900$ MeV from the Monte Carlo method.

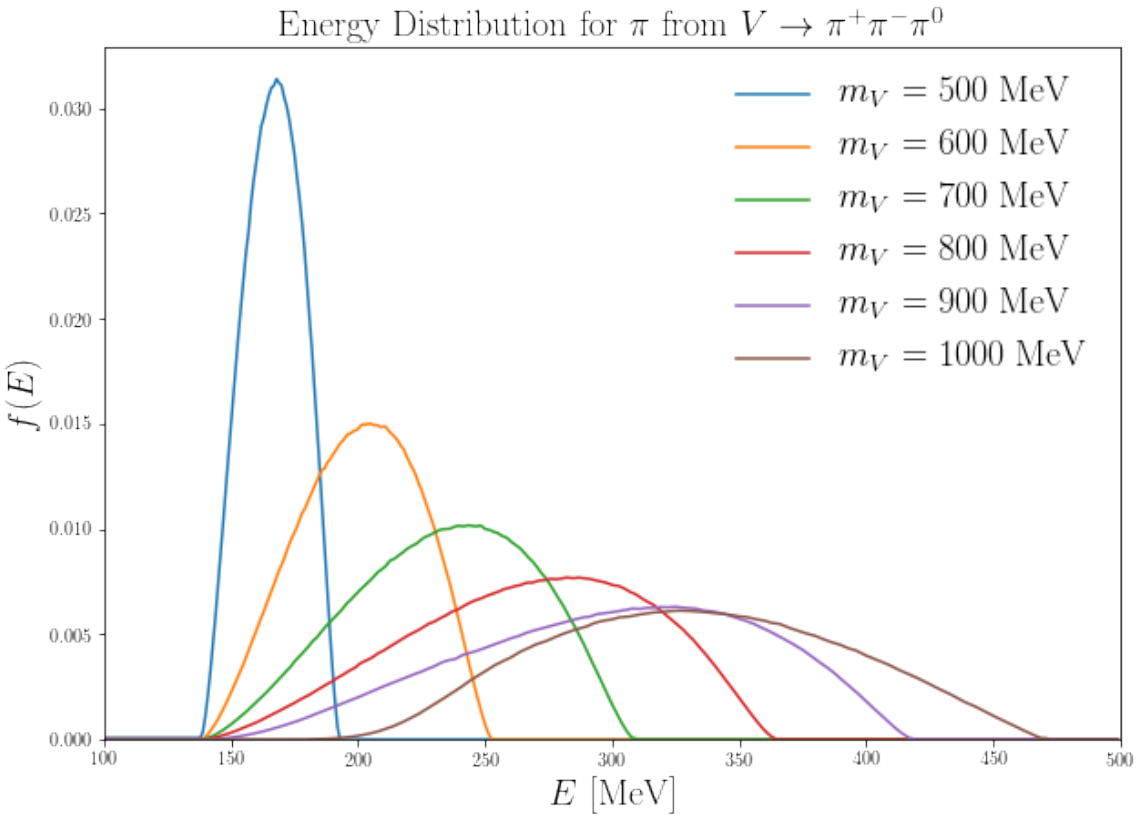

Figure 3.13: Energy distribution for a pion (charged or uncharged) from the decay $V \to \pi^+\pi^-\pi^0$.

The distributions of the energy and momentum of the pions were averaged to obtain an overall energy and momentum distribution. The results of the distribution can be seen in Figure 3.13 for various masses of V.

With the energy distribution of the pions calculated, they can be used in further

analysis to obtain energy distributions for the decay products of the pions. The method of obtaining the final energy spectra is similar to the $V \to \pi^0\gamma$ and $V \to \pi^+\pi^-$ channels. Where the final distribution of the photons, electrons and positrons are weighted by the energy distributions generated above. The results for this channel are shown in Figures 3.14 and 3.15.

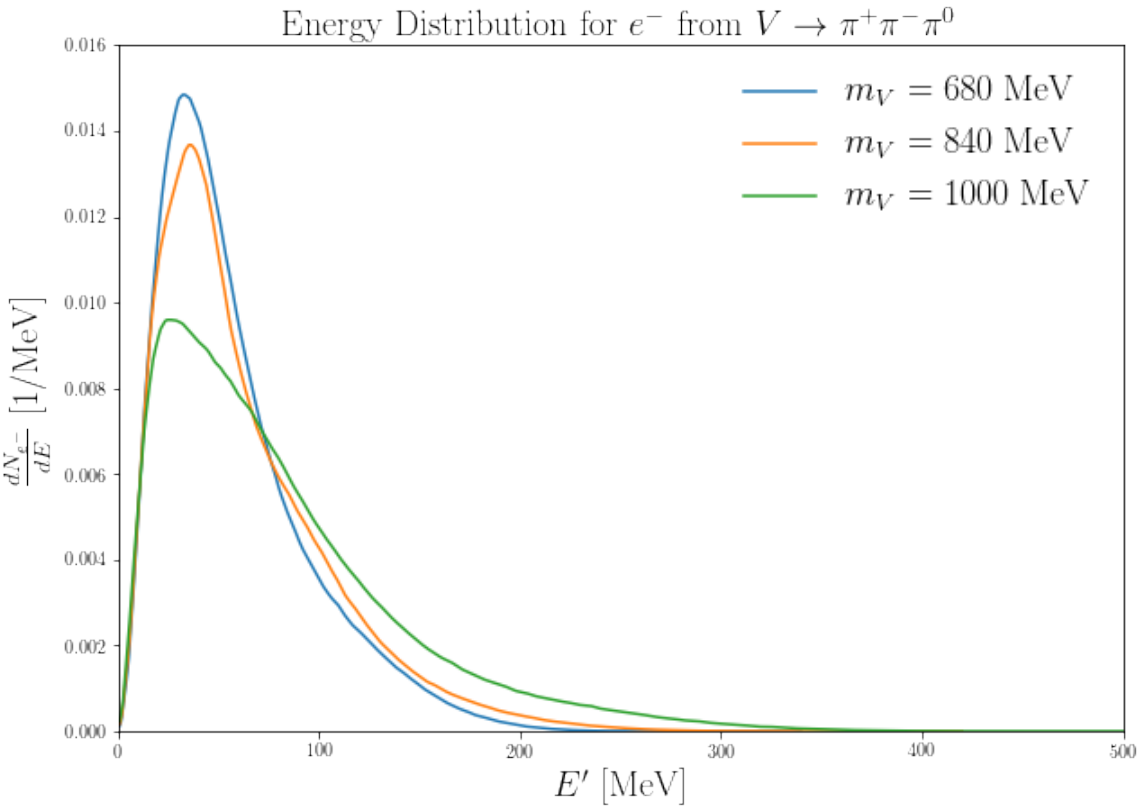

Figure 3.14: Electron energy distribution from $V \to \pi^+\pi^-\pi^0$.

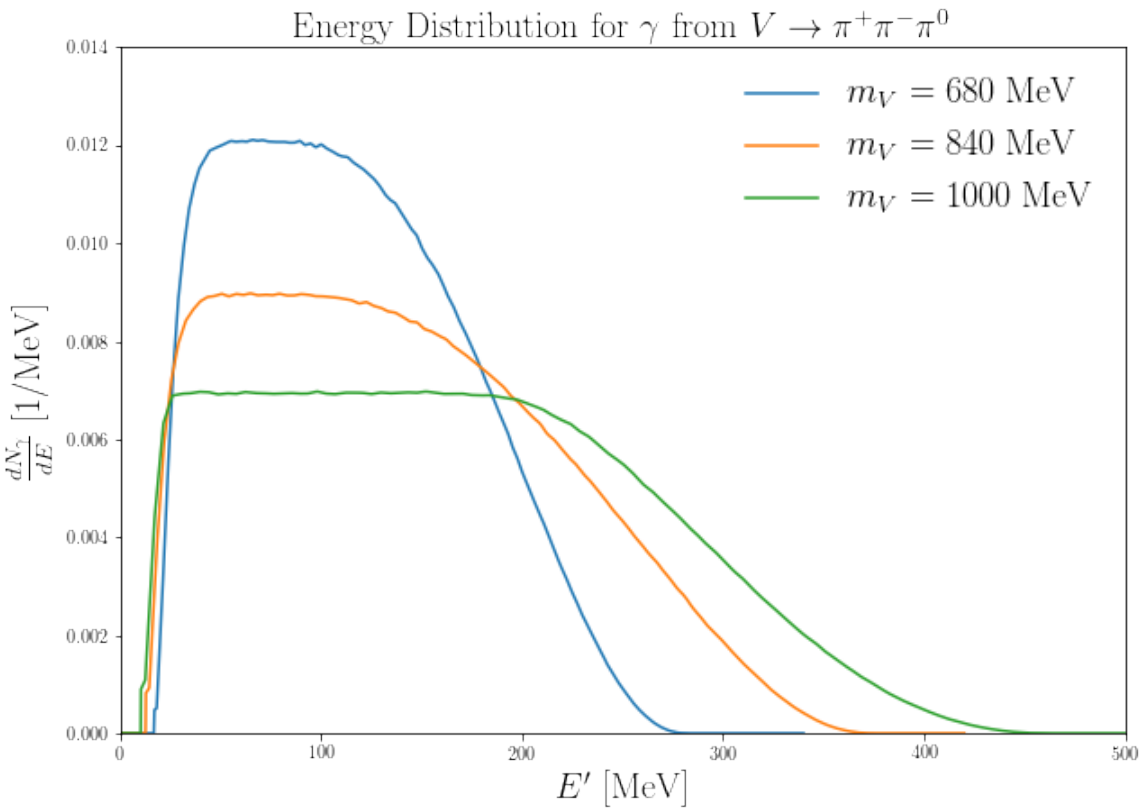

Figure 3.15: Photon energy distribution from $V \to \pi^+\pi^-\pi^0$.

Chapter 4

Cosmological Constraints on Electromagnetic Energy Injection

By examining the dark vector models up to 1 GeV, hadronic channels had to be introduced to ensure the proper behaviour for higher masses. My work centered around calculating the branching ratios for each model and EM energy spectra for each channel. This chapter features the results of applying my results to the work of my collaborators, David Morrissey and Graham White, by constraining their calculations to measurements from BBN and the CMB power spectrum.

4.1 Big Bang Nucleosynthesis

The channels described in the previous Chapter produce photons, electron, or positrons. These particles can cause an EM cascade to occur in the Intergalactic Medium (IGM). If these decays happen at an early time in the Universe when elements are first being formed, the cascades can have enough energy to destroy the elements forming. This is known as photodissociation, and can change the abundance of elements formed in the early Universe. The EM cascade can also deposit its energy into the IGM. If the EM cascades occur at a later times after BBN has completed the effects of the cascades can be seen in the CMB.

To find the energy spectra for photons, electrons and positrons up to the leading order for the relevant decay channels and models mentioned one can compute using

$$\frac{dN_a}{dE} = \sum_c \mathrm{Br}_c \frac{dN_a^{(c)}}{dE}, \quad a = \gamma, e \tag{4.1}$$

Where the spectrum for e is the sum of electrons and positrons. To compute the full spectra, non-leading order terms from final state radiation (FSR) for each channel are necessary and described in full detail in [60]. We only examine EM effects in the early Universe which correspond to times after $\sim 10^4 s$ which is when pions stop in the plasma before decaying. At earlier times, pions can induce hadronic effects before decaying [61]; however, the focus of this thesis is on EM effects only.

Big Bang Nucleosynthesis (BBN) is the process in the early Universe when light elements were created and has been a successful tool in constraining dark matter models. When the dark vectors decay, they inject photons, electrons and positrons which interact with the IGM creating EM cascades. When the temperature of the IGM is $T \in [1\text{ eV}, 10\text{keV}]$, the most noticeable reactions are

- Photon photon pair production (4P): $\gamma + \gamma_{BG} \to e^+ + e^-$
- Photon photon scattering (PP): $\gamma + \gamma_{BG} \to \gamma + \gamma$
- Pair creation on Nuclei (PCN): $\gamma + N_{BG} \to N_{BG} + e^+ + e^-$
- Compton Scattering (CS): $\gamma + e^-_{BG} \to \gamma + e^-$
- Inverse Compton (IC): $e^\pm + \gamma_{BG} \to e^\pm + \gamma$
- Final state radiation (FSR): $X \to e^+ + e^- + \gamma$

Where the BG subscript is used for particles from the IGM. The most important reaction for the photon cascade is 4P and for electrons and positrons it is IC. These cascades are created very quickly when compared to the scattering of the cascades off of the light elements, and as such the cascades can be treated as a source for photodissociation for the light elements [62].

To understand where the energy spectra are introduced one can start by defining the differential number density per unit energy of particle a.

$$\mathcal{N}_a = \frac{dn_a}{dE}, \quad a = \gamma, e \tag{4.2}$$

Where a is either photons or the sum of electrons and positrons. With this quantity the Boltzmann equation for the evolution of the number density may be define as

Process	**Threshold** (MeV)	**Peak Value** (mb)
$D + \gamma \rightarrow p + n$ [63]	2.220	2.47
$^3He + \gamma \rightarrow p + p + n$ [64]	2.486	1.02
$^3He + \gamma \rightarrow D + p$ [64]	5.490	1.18
$T + \gamma \rightarrow n + D$ [65, 66]	6.260	0.818
$T + \gamma \rightarrow n + n + p$ [66]	8.480	0.878
$^4He + \gamma \rightarrow T + p$ [67]	19.81	1.31
$^4He + \gamma \rightarrow ^3He + n$ [68, 69]	20.58	1.28
$^4He + \gamma \rightarrow D + D$ [70]	23.85	0.0051
$^4He + \gamma \rightarrow n + p + D$ [67]	26.07	0.182

Table 4.1: Nuclear processes that are relevant for the photodissociation effects from an EM cascade, as well as threshold energies and peak cross sections [62]. The three most important processes are the deuterium depletion, helium 4 into helium 3 and helium 4 into deuterium.

$$\frac{d\mathcal{N}_a}{dt}(E) = -\Gamma_a(E)\mathcal{N}_a(E) + \mathcal{S}_a(E) \tag{4.3}$$

Where Γ_a is the relaxation rate at energy E, and S_a describes all sources injecting energy at E both fully derived in the Appendix of [62]. Typically there is a Hubble dilution term included but since the relaxation rate is much faster, the Hubble term is omitted [62]. Using the assumption from above that the relaxation rate is much smaller than the interaction with nuclei from BBN, a quasistatic approximation can be made $d\mathcal{N}_a/dt \rightarrow 0$, [62, 71] which when applying to the Boltzmann equation a solution can be found.

$$\mathcal{N}_a(E) = \frac{\mathcal{S}_a(E)}{\Gamma_a(E)} \tag{4.4}$$

The source terms come from direct injection from decaying particles and transfer reactions moving from higher energy E' to a lower energy E. Therefore, the source term can be described as

$$\mathcal{S}_a(E) = R\frac{dN_a}{dE} + \sum_b \int_E^{E_X} dE' K_{ab}(E, E')\mathcal{N}_b(E') \tag{4.5}$$

Where $\frac{dN_a}{dE}$ is defined in Eq. 4.1, the decay of V limits the maximum energy in the cascade to be $E_X \leq m_V/2$ and K_{ab} is the transfer kernel for the reactions shown above and is fully explained and derived in the Appendix of [62]. Finally, R is the injection rate defined as

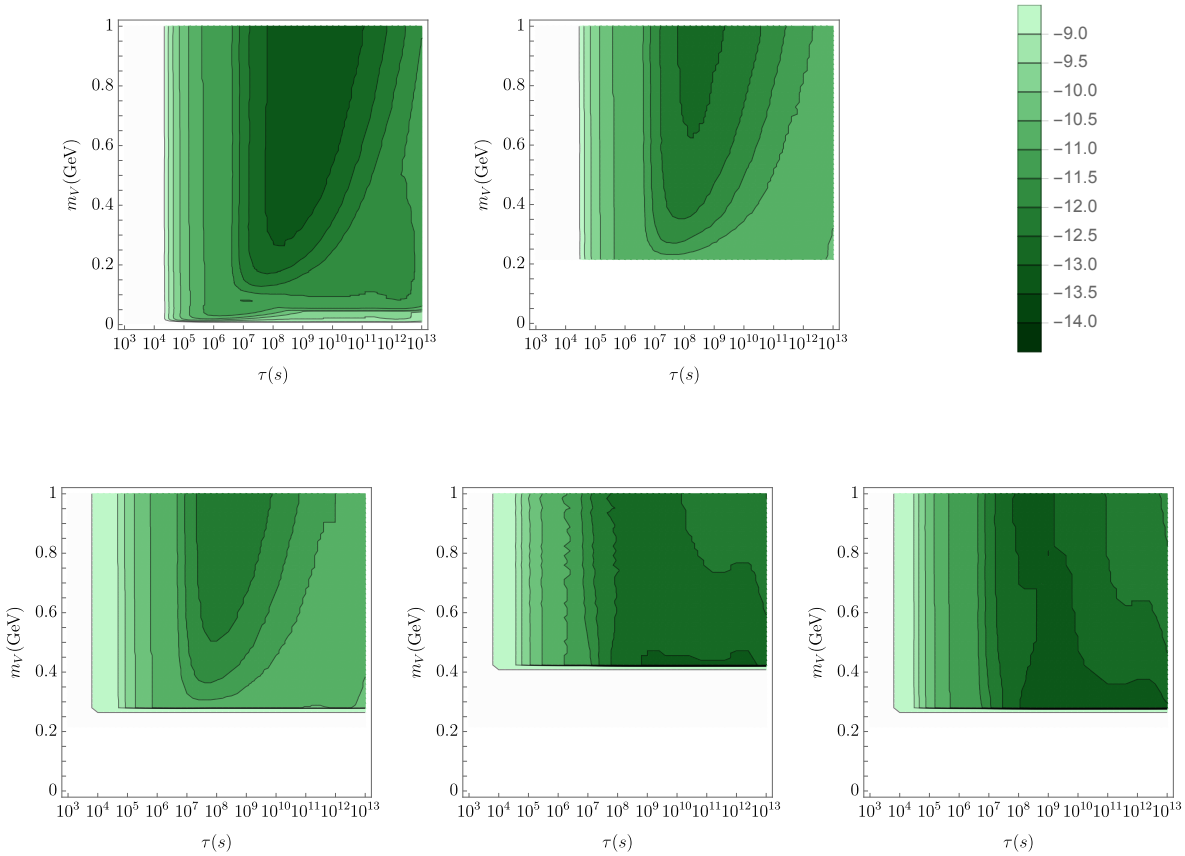

Figure 4.1: BBN limits for $\log_{10}(m_V Y_V/\mathrm{GeV})$ in the parameter space of mass and lifetime on exclusive decay channels $V \to e^+e^-$ (upper left), $V \to \mu^+\mu^-$ (upper right), $V \to \pi^+\pi^-$ (lower left), $V \to \pi^+\pi^-\pi^0$ (lower middle), $V \to \pi^0\gamma$ (lower right).

$$R(t) = \frac{n_V^0}{\tau_V} e^{-t/\tau_V} \tag{4.6}$$

Where n_V^0 is the number density of the vector boson before decays occur and τ_V is the lifetime of the vector boson.

For BBN, the evolution of the photon cascade is of interest since it is responsible for the photodissociation of light elements. This occurs at low energies and at theses energies the electron cascade is negligible due to the IC process. However, when one examines higher energies the IC effect becomes stronger and eventually matches the photon cascade effects. Thus, a universality is achieved for EM cascades when above a threshold energy and the EM spectra is required when below it.

$$E_{\text{thres.}} = \frac{m_e^2}{22T} \tag{4.7}$$

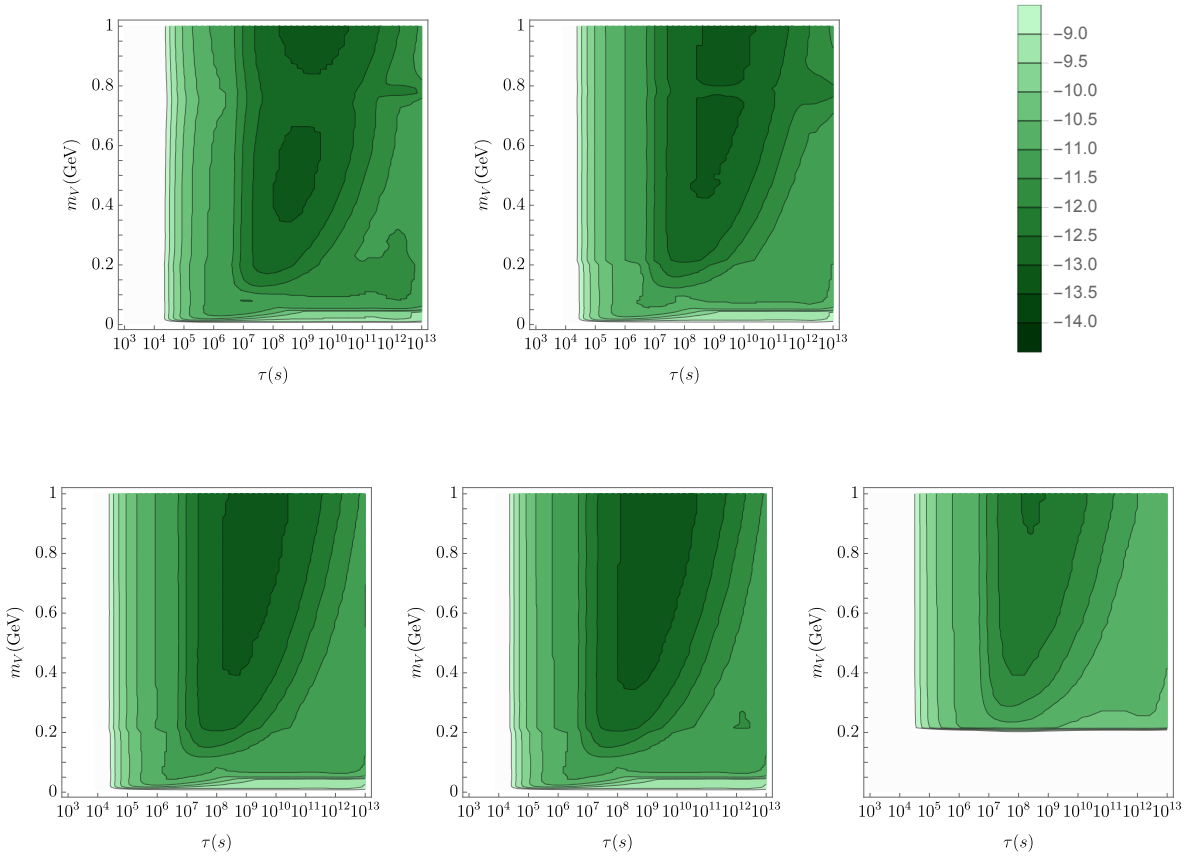

Figure 4.2: BBN limits for $\log_{10}(m_V Y_V/\text{GeV})$ in the parameter space of mass and lifetime on models A' (upper left), $B-L$ (upper right), $L_\mu - L_e$ (lower left), $L_e - L_\tau$ (lower middle), $L_\mu - L_\tau$ (lower right).

Using the photon cascade, the Boltzmann equation can be used to describe the evolution of the light elements

$$\frac{dY_A}{dt} = \sum_i Y_i \int_0^\infty dE_\gamma \mathcal{N}_\gamma(E_\gamma)\sigma_{\gamma+i\to A}(E_\gamma) - Y_A \sum_f \int_0^\infty dE_\gamma \mathcal{N}_\gamma(E_\gamma)\sigma_{\gamma+A\to f}(E_\gamma) \tag{4.8}$$

Where $\mathcal{N}_\gamma$ is the photon cascade spectrum, A and the sums run over the relevant isotopes and $Y_A = \frac{n_A}{s}$ are number densities normalized to the entropy density. The most important nuclear species for the analysis were hydrogen, deuterium, tritium, helium 3, and helium 4. Table 4.1 describes the photodissociation of the species in question.

Eq. 4.8 can be solved for the interweaving equations by switching time into redshift z and utilizing abundances of light elements predicted by `PArthENoPE` [72, 73] and measurements from [74, 75, 76]. The uncertainties for the abundances were added in

quadrature of the theoretical and measured quantities.

$$Y_p = 0.245 \pm 0.004 \tag{4.9}$$

$$\frac{n_{\mathrm{D}}}{n_{\mathrm{H}}} = (2.53 \pm 0.05) \times 10^{-5} \tag{4.10}$$

$$\frac{n_{^3\mathrm{He}}}{n_{\mathrm{H}}} = (1.0 \pm 0.5) \times 10^{-5} \tag{4.11}$$

Where Y_p is the helium mass fraction, $\frac{n_{\mathrm{D}}}{n_{\mathrm{H}}}$ is the abundance ratio of deuterium to hydrogen, and $\frac{n_{^3\mathrm{He}}}{n_{\mathrm{H}}}$ is the abundance ratio of helium 3 to hydrogen. With these limits in place, the parameter space for the mass m_V, lifetime τ_V, and predecay yield $m_V Y_V$ of the dark vector can be found for either exclusive decay channels or for the five dark vectors shown in Figures 4.1 and 4.2.

Comparing the top left plots in Figures 4.1 and 4.2, one can see that in the regime when $m_V < 2m_\mu$, the same $m_V Y_V$ is obtained. Not only that, but compared to Figure 8 in [62] the same results are seen for the injection of an electron and positron up to 100 MeV. The inclusion of the branching ratio and energy distributions allows the extension of the results obtained in [62] to higher masses of the dark vector decay. Thus, a larger range of parameter space for sub-GeV dark vector on the mass and lifetime can be constrained by measurements using BBN. Examining Figure 4.2 further, the spikes from the hadronic resosnances can be seen around $m_V \approx 770$ MeV.

4.2 CMB

The decay of the dark vectors before recombination can alter the power spectra of the CMB due to the EM energy injected. The CMB is a very good probe since its calculations follow very well understood physics. Thus, detecting small deviations from the expected signal can be held at high significance [77]. Injecting a small amount of energy allows for small modification and allows it to be consistent with the ΛCDM model, but if the injected energy is too large it become inconsistent with the model. Thus, one can see the CMB is a powerful method to constrain the results of the EM energy spectra from the decay of sub-GeV dark vectors. If the energy is injected at a later time anistropies can be made which would further distort the CMB power spectra, further supporting an unknown source of energy injection.

The energy injected from the decaying dark matter is not immediately deposited in the IGM, instead the energy is deposited over a period of time. Not only is the energy

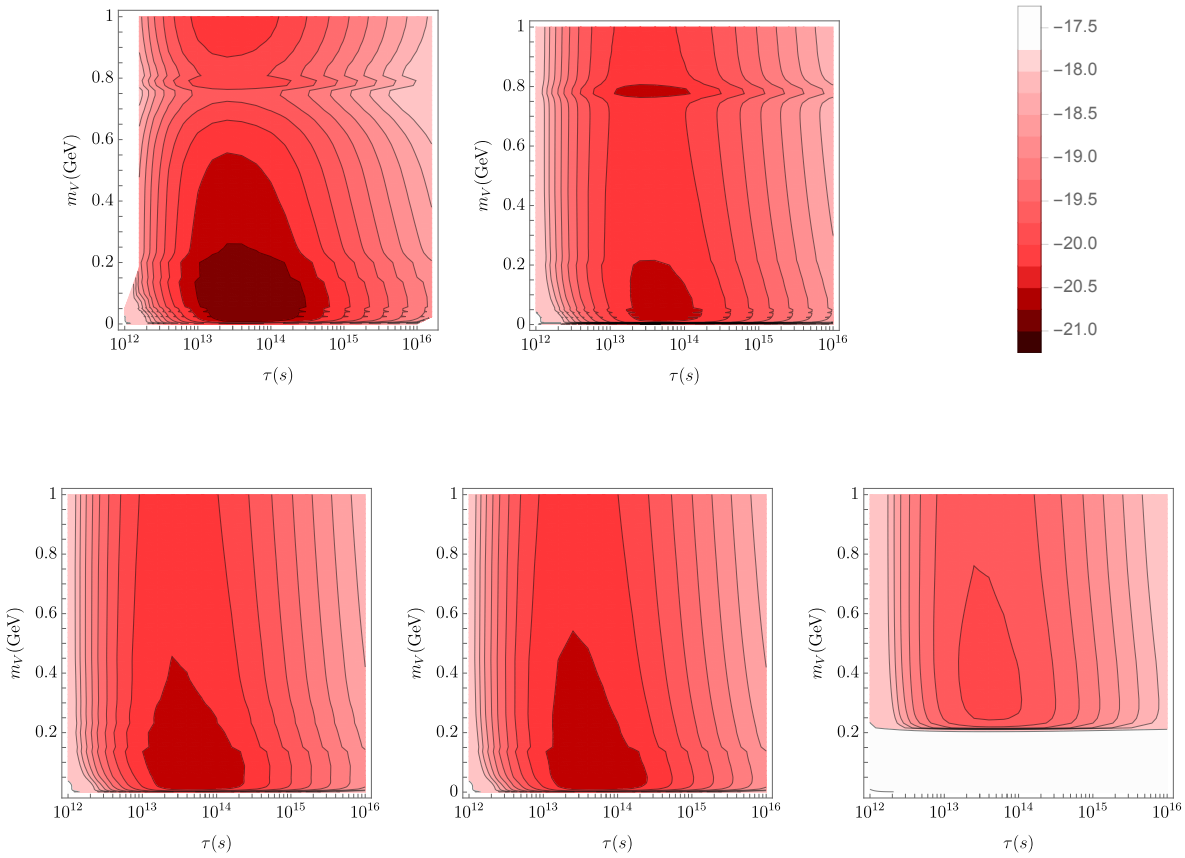

Figure 4.3: CMB limits for $\log_{10}(m_V Y_V/\text{GeV})$ based on Planck measurments in the parameter space of mass and lifetime on models A' (upper left), $B-L$ (upper right), $L_\mu - L_e$ (lower left), $L_e - L_\tau$ (lower middle), $L_\mu - L_\tau$ (lower right).

not injected immediately, not all of the energy will be deposited into the expected source, thus the efficiency of depositing energy is necessary too [78, 79]. The injected energy comes from the decay of the dark vector

$$\left(\frac{dE}{dz}\right)_{\text{inj.}} = m_V R(t(z)) \tag{4.12}$$

Where R is defined in Eq. 4.6, and t is the injection time transformed into a function of redshift z. This can all be summarized by a complicated function f'_c, which is the ratio between the energy deposited to channel c at redshift z and energy injected at redshift z'.

$$\left(\frac{dE}{dz}\right)_{c,\text{dep.}} = f'_c(z)\left(\frac{dE}{dz}\right)_{\text{inj.}} = f_c(z)\frac{m_V n_V^0}{\tau_V} \tag{4.13}$$

The variable c is for the channels which consist of ionization of hydrogen ions,

ionization of helium ions, Lyman-α excitation of hydrogen atoms, heating of the IGM, and energy converted into continuum photons that are observed as distortions of the CMB energy spectrum. The function $f_c(z)$ for decays can be described by [78]

$$f_c(z) = \frac{H(z)\sum_{\mathrm{a}}\int_{\ln(1+z)}^{\infty}\frac{d\ln(1+z')}{H(z')}\int T_c(z',z,E)E\frac{dN_a}{dE}e^{-t(z')/\tau_V}dE}{\sum_{\mathrm{a}}\int E\frac{dN_a}{dE}dE} \tag{4.14}$$

Where $H(z)$ is the hubble parameter, a sums over γ and e, $T_c(z', z, E)$ are complex transfer function that described the fraction of energy injected at redshift z' that is deposited at redshift z into channel c due to an injection of particles with individual energy E which are fully explained in [78, 79]. The next term $t(z')$ is the time at injected redshift z', τ_V is the lifetime of the dark vector and $\frac{dN_a}{dE}$ is defined in Eq. 4.1.

Figure 4.3 displays the deviation of the CMB power spectrum relative to Planck measurements in the parameter space of the mass m_V, lifetime τ_V and pre-decay yield $m_V Y_V$ of the dark vector. The small deviations from the Planck measurements allow a larger parameter space to be examined for sub-GeV dark vectors. The deviation present around $m_V \approx 770$ MeV for A' and $B-L$ come from the spike of the hadronic channels in their branching ratios. Interestingly, the effect of the $\pi^+\pi^-$ channel can be observed by comparing the two models. There are larger deviations if it is included (A' model) and much smaller deviations if excluded ($B-L$ model). Focusing on the A' model at this mass there is a reduction in the constraint due to muons injecting less EM energy than electrons, and pions injecting even less than muons. The final three models introduce small deviations but with no interesting features around the meson resonances since those branching ratios were set to zero.

4.3 Production of Dark Vectors

The previous Chapter showed that the dark vectors can decay into several different channels. The opposite is also just as viable where particles can annihilate into the dark vector with the same decay width, known as freezing in. This is one of many production mechanisms with freeze in being the minimal production mechanism [80]. This production mechanism also corresponds to a minimal density of dark vectors, while only assuming that the dark vector is reheated once the temperature is above its mass. Freeze in occurs before freeze out, since at freeze out dark matter decouples resulting in no more interactions. The density of the dark vector can be calculated

by using the Boltzmann equation, but this time, having particles annihilate into the dark vector. Explained in [48, 81], it takes the form

$$s\dot{Y}_V = \mathcal{C}\left[f_V\right] \tag{4.15}$$

Where $\mathcal{C}$ is the standard collision term [81], and in the case for underpopulated dark vectors assuming Maxwell-Boltzmann distributions for the particle and ignoring thermal corrections.

$$\mathcal{C}[f_V] = \frac{3}{2\pi^2}\Gamma_V m_V^2 T K_1\left(\frac{m_V}{T}\right) \tag{4.16}$$

Where Γ_V is the total decay width of the dark vector, T is the temperature of the IGM, and K_1 is the modified Bessel function of the first kind. This can be solved by using the substituion $x = m_V/T$ which removes time from the equation. Solving this below and above the QCD phase transition, $\Lambda_{\text{QCD}} \approx 157$ MeV, one can find the net yield

$$Y_V = (Y_V)_I + (Y_V)_{II} \tag{4.17}$$

With

$$(Y_V)_I = \frac{3}{2\pi^2} m_V^3 \tilde{\Gamma}_V \int_0^{x_{\text{QCD}}} dx \frac{K_1(x)}{x^2 sH} \tag{4.18}$$

$$(Y_V)_{II} = \frac{3}{2\pi^2} m_V^3 \Gamma_V \int_{x_{\text{QCD}}}^{\infty} dx \frac{K_1(x)}{x^2 sH} \tag{4.19}$$

Where $\tilde{\Gamma}_V$ is the total decay width into leptons and quark pairs below the Λ_{QCD} limit, and $x_{\text{QCD}} = m_V/\Lambda_{\text{QCD}}$. The quantity Y_V is important as it is used to describe the dark vector yield before the particle decays in the early Universe. To determine the decay yield, one multiplies the yield by m_V. Finally, a new definition of the effective coupling constant can be constructed so the results can be compared to other works.

$$\epsilon_{eff} = \sqrt{\alpha_V/\alpha_{\text{em}}} \tag{4.20}$$

New constraints have been set on the lifetime, mass and coupling constant of dark vectors for various models and shown in Figures 4.1, 4.2 and 4.3. The constraints can be summarized by plotting in a new parameter space of the effective coupling against the mass of the dark vector boson with the thermal freeze in abundance of the dark vector displayed in Figure 4.4. Upon examining the figure, one can see that as the effective coupling becomes weaker, the lifetime becomes longer. This makes sense since a stronger coupling to the SM would result in a larger abundance of SM

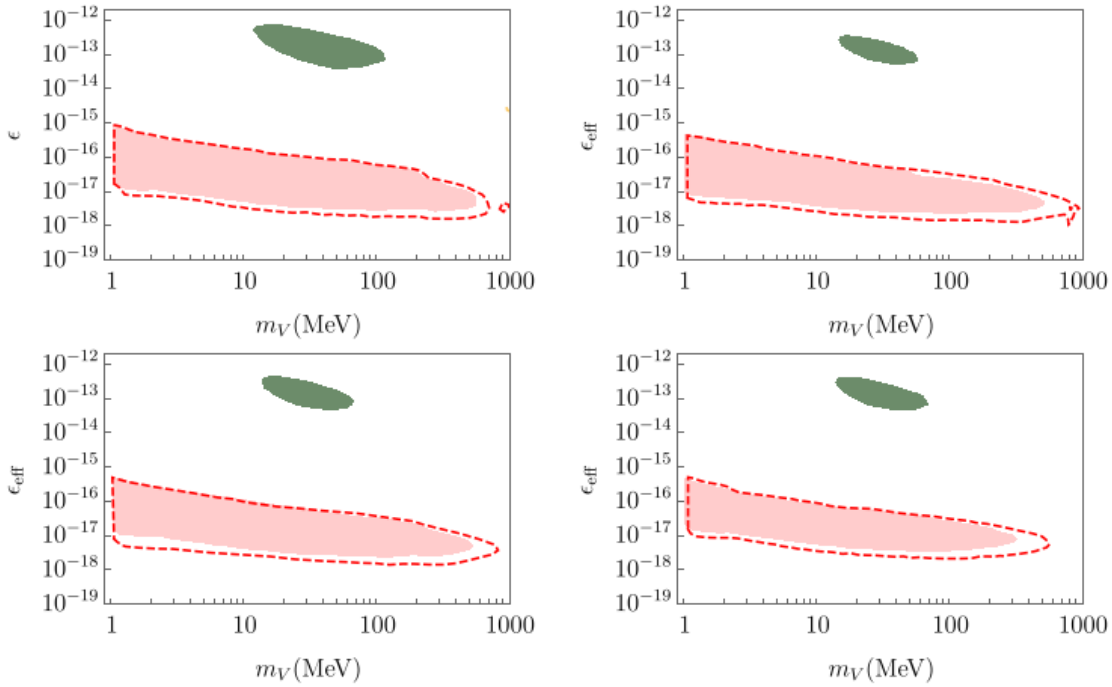

Figure 4.4: Cosmological limits on dark vectors from EM energy injection as a function of the dark vector mass m_V and effective coupling ϵ_{eff} assuming a thermal freeze-in abundance. The dark vector varieties shown are A' (upper left), $B-L$ (upper right), $L_\mu - L_e$ (lower left), and $L_e - L_\tau$ (lower right). The shaded green regions indicate the exclusions from BBN due to photodissociation, the shaded red regions show the exclusion from the CMB power spectrum measured by Planck, the dashed red contours indicate the projected limits for a cosmic variance limited experiment.

particles to be present; therefore, a larger effect would be seen in both BBN and CMB measurements. It can also be seen that the upper part of both wedges follow a lifetime curve for the dark vector. The BBN contour is bound above by $\tau_V = 10^4$ sec, and CMB is bounded by $\tau_V = 10^{13}$ sec. These are the minimum lifetime required for the EM effects to be observed. As for the lower part of the wedges this cut off appears due to the coupling becoming too weak for the EM effects to be significant on BBN and the CMB power spectrum.

4.4 Cosmic X-rays

Under the assumption that decaying dark matter can produce SM particles, a positron can be one of the final states. The positron can interact with an electron from the IGM, and the two particles can annihilate into a photon which then propagates

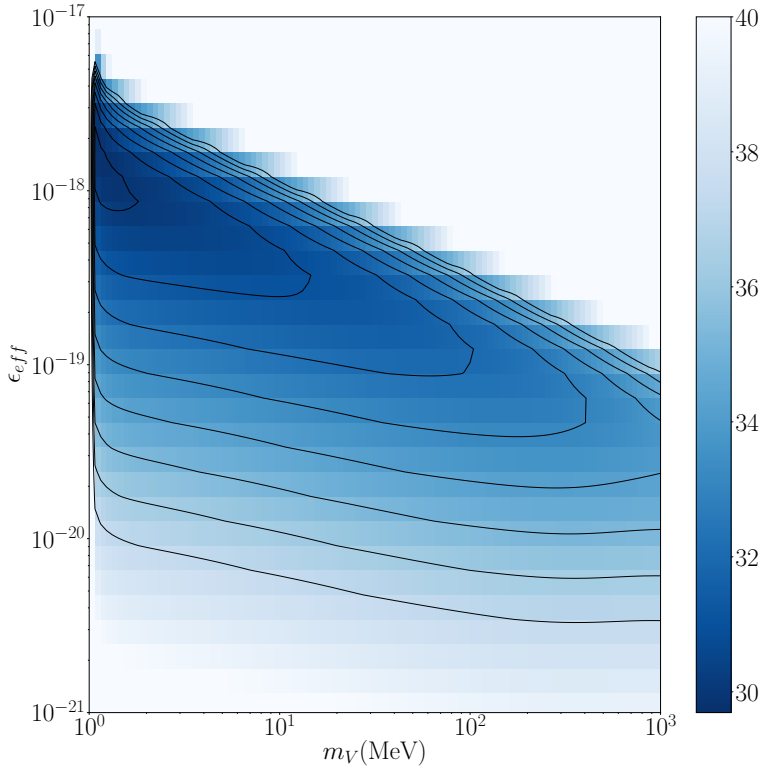

Figure 4.5: Effective lifetime contour plots, $\log_{10}(\tau_{eff}/\text{sec})$, for cold dark matter compared to an exclusive e^+e^- decay in the parameter space of the mass m_V and effective coupling ϵ_{eff} of the dark vector. The inner most black line corresponds to an τ_{eff} of 10^{30} sec and the outermost black line corresponds to 10^{38} sec.

through the Universe. This interaction could account for unknown signals not produced from stars, nor predicted from the SM. Some photons produced from the decay of dark matter can have the same effect; however, this section focuses on positron creation from decaying dark matter.

To set lower bounds on dark matter decaying exclusively to e^+e^-, the energy injection of dark matter can be compared to a simplified model for the dark vector decaying exclusively to e^+e^-. But first, the equation for energy injection from a particle of mass m and lifetime τ is needed.

$$E_{inj} = mYs_0\frac{1}{\tau}\exp(-t_{Uni}/\tau) \tag{4.21}$$

With $t_{Uni} \approx 4.35 \times 10^{17}$ s being the age of the Universe. To simplfy the comparison, the lifetime for dark matter can be changed into an effective lifetime τ_{eff}, which is set to be much larger than t_{Uni}. The effective lifetime is the lifetime that dark matter would need to produce the equivalent signal of the dark vector today. It should be noted that the dark vector lifetime will be much smaller than the effective lifetime.

$$m_V Y_V s_0 \frac{1}{\tau_V} \exp(-t_{Uni}/\tau_V) = (mYs_0)_{DM} \frac{1}{\tau_{eff}} \exp(-t_{Uni}/\tau_{eff}) \tag{4.22}$$

Using $\tau_{eff} \gg t_{Uni}$ the equation becomes

$$\tau_{eff} = \frac{(\Omega_{CDM}\rho_c)\tau_V \exp(-t_{Uni}/\tau_V)}{m_V Y_V s_0} \tag{4.23}$$

Where $(\Omega_{CDM}\rho_c) = (mYs_0)_{DM} \approx 1.24 \times 10^{-7}\text{MeV/cm}^3$. Figure 4.5 gives a lower bound of 10^{30} sec for the effective lifetime of dark matter. As for the sharp drop off seen where the blue fades away quickly, this is due to the decoupling of dark matter in the early Universe.

Future experiments will be able to constrain the effective lifetime, but for now more data is required from cosmic X-rays to determine the sensitivity. The bounds found from this are reasonable given that current experiments don't rule out the effective lifetime and future experiments will depend on the energy spectra from decays.

Chapter 5

Conclusion

From cosmological evidence, it is clear that dark matter is present in the Universe. If it is a particle, it can have full-strength weak interactions with the SM (i.e. WIMPs) but it is must have very tiny couplings to the SM through the strong and electromagnetic forces. Extensions to the SM must be made to accommodate new dark forces. To interact with the forces, a portal is necessary for the dark forces, which is the motivation for dark vectors. The dark vectors have some interaction with the SM particles, either through the kinetic mixing of the photon or coupling to anomalous currents. This thesis explored the dark photon kinetically mixing with the photon, and four currents of $B - L$, $L_\mu - L_e$, $L_e - L_\tau$, and $L_\mu - L_\tau$. The branching ratio for these models was calculated in the sub-GeV region. The electromagnetic energy spectrum for each channel was calculated as well. Together, the two could give the total electromagnetic spectrum for both the photon and the sum of electrons and positrons. Understanding the behaviour of these models in the sub-GeV region allowed the extension of parameter space. With constraints from BBN and the CMB, the parameter space for the lifetime and mass of the decaying dark vectors were constrained. Cosmic X-rays were also explored and limits were set on dark matter decaying with a large lifetime. The results of BBN and CMB measurements were summarized in Figure 4.4 which parametrize the limits to the effective coupling constant and mass of the dark vector. The models were extended beyond their previous known limits allowing more areas for experiments to search.

Future works could involve extending beyond the sub-GeV limit including complex hadron resonances, and including more decay channels for the cosmic X-rays analysis. The Lithium abundance issue is another project that could be explored.

Bibliography

[1] G. Altarelli, *The Higgs and the Excessive Success of the Standard Model*, *Frascati Phys. Ser.* **58** (2014) 102, [1407.2122].

[2] T. Shears, *The Standard Model*, *Phil. Trans. Roy. Soc. Lond.* **A370** (2012) 805–817.

[3] F. Englert and R. Brout, *Broken Symmetry and the Mass of Gauge Vector Mesons*, *Phys. Rev. Lett.* **13** (1964) 321–323.

[4] ATLAS collaboration, G. Aad et al., *Observation of a new particle in the search for the Standard Model Higgs boson with the ATLAS detector at the LHC*, *Phys. Lett.* **B716** (2012) 1–29, [1207.7214].

[5] M. Nemevsek, G. Senjanovic and V. Tello, *Connecting Dirac and Majorana Neutrino Mass Matrices in the Minimal Left-Right Symmetric Model*, *Phys. Rev. Lett.* **110** (2013) 151802, [1211.2837].

[6] A. Capolupo and S. M. Giampaolo, *Neutrino nature, total and geometric phase*, *J. Phys. Conf. Ser.* **1275** (2019) 012053, [1904.11249].

[7] A. Capolupo, S. M. Giampaolo, B. C. Hiesmayr and G. Vitiello, *Geometric phase of neutrinos: differences between Dirac and Majorana neutrinos*, *Phys. Lett.* **B780** (2018) 216–220, [1610.08679].

[8] V. Barger, K. Hagiwara and Y.-J. Zheng, *Probing the top Yukawa coupling at the LHC via associated production of single top and Higgs*, 1912.11795.

[9] M. E. Peskin and D. V. Schroeder, *An Introduction to quantum field theory*. Addison-Wesley, Reading, USA, 1995.

[10] O. Darrigol, *The magic of Feynman's QED: from field-less electrodynamics to the Feynman diagrams*, *Eur. Phys. J.* **H44** (2019) 349–369.

[11] F. Zwicky, *Die Rotverschiebung von extragalaktischen Nebeln*, *Helv. Phys. Acta* **6** (1933) 110–127.

[12] K. Begeman, A. Broeils and R. Sanders, *Extended rotation curves of spiral galaxies - dark haloes and modified dynamics*, *Monthly Notices of the Royal Astronomical Society* **249** (1991) 523–537.

[13] J. Bovy and H.-W. Rix, *A direct dynamical measurement of the milky way's disk surface density profile, disk scale length, and dark matter profile at 4 kpc* $\lesssim r \lesssim$ *9 kpc*, *The Astrophysical Journal* **779** (2013) 115.

[14] B. Famaey, *Dark Matter in the Milky Way*, *PoS* **FFP14** (2016) 051, [1501.01788].

[15] M. Bauer and T. Plehn, *Yet Another Introduction to Dark Matter*, *Lect. Notes Phys.* **959** (2019) pp.–, [1705.01987].

[16] G. F. Smoot et al., *First results of the COBE satellite measurement of the anisotropy of the cosmic microwave background radiation*, in *Proceedings, 2nd Rencontre de Blois on Physical Cosmology: Blois, France, August 28-September 1, 1990*, pp. 105–120, 1991.

[17] L. Page, E. Komatsu, J. L. Weiland, D. Larson, A. Kogut, M. Halpern et al., *Nine-year wilkinson microwave anisotropy probe (wmap) observations: Final maps and results*, *The Astrophysical Journal Supplement Series* **208** (2013;2012;) .

[18] Planck collaboration, N. Aghanim et al., *Planck 2018 results. VI. Cosmological parameters*, 1807.06209.

[19] R. O. Ramos and L. A. da Silva, *Power spectrum for inflation models with quantum and thermal noises*, *JCAP* **1303** (2013) 032, [1302.3544].

[20] A. M. J. Smith, *Mock Catalogues for Large Scale Structure Surveys and DESI*. PhD thesis, 2018.

[21] N. Drakos, *The Evolution of Dark Matter Haloes in Mergers*. PhD thesis, U. Waterloo (main), 2019.

[22] L. Heurtier and H. Partouche, *Spontaneous Freeze Out of Dark Matter From an Early Thermal Phase Transition*, 1912.02828.

[23] M. Dutra, *Freeze-in production of dark matter through spin-1 and spin-2 portals*, *PoS* **LeptonPhoton2019** (2019) 076, [1911.11844].

[24] P. Mocz et al., *Galaxy Formation with BECDM - II. Cosmic Filaments and First Galaxies*, 1911.05746.

[25] C. Chatterjee, *Dark Matter Self Interactions and its Impact on Large Scale Structures*, 1901.05658.

[26] Planck collaboration, P. A. R. Ade et al., *Planck 2015 results. XIII. Cosmological parameters*, *Astron. Astrophys.* **594** (2016) A13, [1502.01589].

[27] Particle Data Group collaboration, M. Tanabashi et al., *Review of Particle Physics*, *Phys. Rev.* **D98** (2018) 030001.

[28] C. Arina, *Impact of cosmological and astrophysical constraints on dark matter simplified models*, *Front. Astron. Space Sci.* **5** (2018) 30, [1805.04290].

[29] F. S. Queiroz, *Dark Matter Overview: Collider, Direct and Indirect Detection Searches*, in *Proceedings, 51st Rencontres de Moriond on Electroweak Interactions and Unified Theories: La Thuile, Italy, March 12-19, 2016*, pp. 427–436, ARISF, ARISF, 2016. 1605.08788.

[30] K. Cheung, C.-T. Lu, P.-Y. Tseng and T.-C. Yuan, *Collider Constraints on the Dark Matter Interpretation of the CDMS II Results*, 1308.0067.

[31] G. Busoni et al., *Recommendations on presenting LHC searches for missing transverse energy signals using simplified s-channel models of dark matter*, *Phys. Dark Univ.* (2019) 100365, [1603.04156].

[32] J. Kopp, *Collider Limits on Dark Matter*, in *Proceedings, 46th Rencontres de Moriond on Electroweak Interactions and Unified Theories: La Thuile, Italy, March 13-20, 2011*, pp. 411–416, 2011. 1105.3248.

[33] D. Buarque Franzosi, M. T. Frandsen and I. M. Shoemaker, *New or ν missing energy: Discriminating dark matter from neutrino interactions at the LHC*, *Phys. Rev.* **D93** (2016) 095001, [1507.07574].

[34] ATLAS collaboration, G. Aad et al., *Performance of algorithms that reconstruct missing transverse momentum in $\sqrt{s} = 8$ TeV proton-proton collisions in the ATLAS detector*, *Eur. Phys. J.* **C77** (2017) 241, [1609.09324].

[35] D. Hooper, *TASI Lectures on Indirect Searches For Dark Matter*, *PoS* **TASI2018** (2019) 010, [1812.02029].

[36] X.-J. Bi, Y. Gao, J. Guo, N. Houston, T. Li, F. Xu et al., *Axion and dark photon limits from Crab Nebula high energy gamma-rays*, 2002.01796.

[37] A. Bernstein et al., *LBECA: A Low Background Electron Counting Apparatus for Sub-GeV Dark Matter Detection*, in *16th International Conference on Topics in Astroparticle and Underground Physics (TAUP 2019) Toyama, Japan, September 9-13, 2019*, 2020. 2001.09311.

[38] M. Klasen, M. Pohl and G. Sigl, *Indirect and direct search for dark matter*, *Prog. Part. Nucl. Phys.* **85** (2015) 1–32, [1507.03800].

[39] G. Duda, A. Kemper and P. Gondolo, *Model Independent Form Factors for Spin Independent Neutralino-Nucleon Scattering from Elastic Electron Scattering Data*, *JCAP* **0704** (2007) 012, [hep-ph/0608035].

[40] P. Cushman et al., *Working Group Report: WIMP Dark Matter Direct Detection*, in *Proceedings, 2013 Community Summer Study on the Future of U.S. Particle Physics: Snowmass on the Mississippi (CSS2013): Minneapolis, MN, USA, July 29-August 6, 2013*, 2013. 1310.8327.

[41] K. Ichimura, *Solar axion search by annual modulation with XMASS-I detector*, *J. Phys. Conf. Ser.* **1342** (2020) 012068.

[42] M. Kimura, M. Tanaka and K. Yorita, *Status and prospect of the ANKOK project: Low mass WIMP dark matter search using double phase argon detector*, *J. Phys. Conf. Ser.* **1342** (2020) 012069.

[43] Super-Kamiokande collaboration, P. Mijakowski, *Dark Matter Searches at Super-Kamiokande*, *J. Phys. Conf. Ser.* **1342** (2020) 012075.

[44] D. F. Jackson Kimball, D. Budker, J. Eby, M. Pospelov, S. Pustelny, T. Scholtes et al., *Searching for axion stars and Q-balls with a terrestrial magnetometer network*, *Phys. Rev.* **D97** (2018) 043002, [1710.04323].

[45] J. M. Berryman, A. de Gouvêa, K. J. Kelly and Y. Zhang, *Dark Matter and Neutrino Mass from the Smallest Non-Abelian Chiral Dark Sector*, *Phys. Rev.* **D96** (2017) 075010, [1706.02722].

[46] M. D. Campos, F. S. Queiroz, C. E. Yaguna and C. Weniger, *Search for right-handed neutrinos from dark matter annihilation with gamma-rays*, *JCAP* **1707** (2017) 016, [1702.06145].

[47] G. Carosi, A. Friedland, M. Giannotti, M. J. Pivovaroff, J. Ruz and J. K. Vogel, *Probing the axion-photon coupling: phenomenological and experimental perspectives. A snowmass white paper*, in *Proceedings, 2013 Community Summer Study on the Future of U.S. Particle Physics: Snowmass on the Mississippi (CSS2013): Minneapolis, MN, USA, July 29-August 6, 2013*, 2013. 1309.7035.

[48] A. Fradette, M. Pospelov, J. Pradler and A. Ritz, *Cosmological Constraints on Very Dark Photons*, *Phys. Rev.* **D90** (2014) 035022, [1407.0993].

[49] R. Essig et al., *Working Group Report: New Light Weakly Coupled Particles*, in *Proceedings, 2013 Community Summer Study on the Future of U.S. Particle Physics: Snowmass on the Mississippi (CSS2013): Minneapolis, MN, USA, July 29-August 6, 2013*, 2013. 1311.0029.

[50] T. Sjostrand, S. Mrenna and P. Z. Skands, *A Brief Introduction to PYTHIA 8.1*, *Comput. Phys. Commun.* **178** (2008) 852–867, [0710.3820].

[51] M. Bauer, P. Foldenauer and J. Jaeckel, *Hunting All the Hidden Photons*, *JHEP* **07** (2018) 094, [1803.05466].

[52] T. Fujiwara, T. Kugo, H. Terao, S. Uehara and K. Yamawaki, *Nonabelian Anomaly and Vector Mesons as Dynamical Gauge Bosons of Hidden Local Symmetries*, *Prog. Theor. Phys.* **73** (1985) 926.

[53] S. Tulin, *New weakly-coupled forces hidden in low-energy QCD*, *Phys. Rev.* **D89** (2014) 114008, [1404.4370].

[54] T. Gherghetta, J. Kersten, K. Olive and M. Pospelov, *Evaluating the price of tiny kinetic mixing*, *Phys. Rev.* **D100** (2019) 095001, [1909.00696].

[55] P. Ilten, Y. Soreq, M. Williams and W. Xue, *Serendipity in dark photon searches*, *JHEP* **06** (2018) 004, [1801.04847].

[56] J. Heeck, *Unbroken $B - L$ symmetry*, *Phys. Lett.* **B739** (2014) 256–262, [1408.6845].

[57] P. Foldenauer, *Dark Sectors from the Hidden Photon Perspective*, in *7th Large Hadron Collider Physics Conference (LHCP 2019) Puebla, Puebla, Mexico, May 20-25, 2019*, 2019. 1907.10630.

[58] H. B. O'Connell, B. C. Pearce, A. W. Thomas and A. G. Williams, *$\rho - \omega$ mixing, vector meson dominance and the pion form-factor*, *Prog. Part. Nucl. Phys.* **39** (1997) 201–252, [hep-ph/9501251].

[59] BaBar collaboration, J. P. Lees et al., *Precise Measurement of the $e^+e^- \to \pi^+\pi^-(\gamma)$ Cross Section with the Initial-State Radiation Method at BABAR*, *Phys. Rev.* **D86** (2012) 032013, [1205.2228].

[60] A. Coogan, L. Morrison and S. Profumo, *Hazma: A Python Toolkit for Studying Indirect Detection of Sub-GeV Dark Matter*, 1907.11846.

[61] M. Pospelov and J. Pradler, *Metastable GeV-scale particles as a solution to the cosmological lithium problem*, *Phys. Rev.* **D82** (2010) 103514, [1006.4172].

[62] L. Forestell, D. E. Morrissey and G. White, *Limits from BBN on Light Electromagnetic Decays*, *JHEP* **01** (2019) 074, [1809.01179].

[63] R. Evans, *The atomic nucleus*. McGraw-Hill, New York, 1955.

[64] A. N. Gorbunov and A. T. Varfolomeev, *Cross Sections of the Reactions $He^3(\gamma, p)D^2$ and $He^3(\gamma, n)2p$*, *Phys. Lett.* **11** (1964) 137.

[65] R. Pfeiffer, *Der Kernphotoeffekt am ^3H (The nuclear photoeffect in ^3H)*, *Zeitschrift für Physik A Hadrons and nuclei* **208** (1968) 129–141.

[66] D. D. Faul, B. L. Berman, P. Meyer and D. L. Olson, *Photodisintegration of H-3*, *Phys. Rev. Lett.* **44** (1980) 129–132.

[67] Yu. M. Arkatov, P. I. Vatset, V. I. Voloshchuk, V. N. Gurev and A. F. Khodyachikh, *Photodisintegration of He-4 Nucleus Down to Threshold of Meson Production*, *Ukr. Fiz. Zh.(Russ. Ed.)* **23** (1978) 1818–1040.

[68] B. L. Berman, R. G. Johnson, J. W. Jury, J. D. Irish, K. G. McNeill and B. J. Thomas, *Photoneutron angular distributions for 4he*, *Canadian Journal of Physics* **53** (1975) 802–811.

[69] C. Malcom, D. Webb, Y. Shin and D. Skopik, *Evidence of a 2+ state from the 4he(γ,n)3he reaction*, *Physics Letters B* **47** (1973) 433 – 435.

[70] R. H. Cyburt, J. R. Ellis, B. D. Fields and K. A. Olive, *Updated nucleosynthesis constraints on unstable relic particles*, *Phys. Rev.* **D67** (2003) 103521, [astro-ph/0211258].

[71] M. Kawasaki and T. Moroi, *Electromagnetic cascade in the early universe and its application to the big bang nucleosynthesis*, *The Astrophysical Journal* **452** (Oct, 1995) 506.

[72] O. Pisanti, A. Cirillo, S. Esposito, F. Iocco, G. Mangano, G. Miele et al., *PArthENoPE: Public Algorithm Evaluating the Nucleosynthesis of Primordial Elements*, *Comput. Phys. Commun.* **178** (2008) 956–971, [0705.0290].

[73] R. Consiglio, P. F. de Salas, G. Mangano, G. Miele, S. Pastor and O. Pisanti, *PArthENoPE reloaded*, *Comput. Phys. Commun.* **233** (2018) 237–242, [1712.04378].

[74] E. Aver, K. A. Olive and E. D. Skillman, *The effects of He I λ10830 on helium abundance determinations*, *JCAP* **1507** (2015) 011, [1503.08146].

[75] R. J. Cooke, M. Pettini and C. C. Steidel, *One Percent Determination of the Primordial Deuterium Abundance*, *Astrophys. J.* **855** (2018) 102, [1710.11129].

[76] J. Geiss and G. Gloeckler, *Isotopic composition of h, he and ne in the protosolar cloud*, *Space Science Reviews* **106** (2003) 3–18.

[77] N. Padmanabhan and D. P. Finkbeiner, *Detecting dark matter annihilation with CMB polarization: Signatures and experimental prospects*, *Phys. Rev.* **D72** (2005) 023508, [astro-ph/0503486].

[78] T. R. Slatyer and C.-L. Wu, *General Constraints on Dark Matter Decay from the Cosmic Microwave Background*, *Phys. Rev.* **D95** (2017) 023010, [1610.06933].

[79] H. Liu, T. R. Slatyer and J. Zavala, *Contributions to cosmic reionization from dark matter annihilation and decay*, *Phys. Rev.* **D94** (2016) 063507, [1604.02457].

[80] F. D'Eramo, N. Fernandez and S. Profumo, *Dark Matter Freeze-in Production in Fast-Expanding Universes*, *JCAP* **1802** (2018) 046, [1712.07453].

[81] E. W. Kolb and M. S. Turner, *The Early Universe*, *Front. Phys.* **69** (1990) 1–547.